Applied Ocean Research 128 (2022) 103305

Contents lists available at ScienceDirect

Applied Ocean Research

journal homepage: www.elsevier.com/locate/apor

Environmental design load for the line force of a point-absorber wave energy converter☆

Zahra Shahroozi [a,*], Malin Göteman [a,c], Erik Nilsson [b,c], Jens Engström [a]

[a] Department of Electrical Engineering, Uppsala University, Ångströmlaboratoriet, Lägerhyddsvägen 1, Uppsala, 752 37, Sweden
[b] Department of Earth Sciences, Uppsala University, Villavägen 16, Uppsala, 752 36, Sweden
[c] Centre of Natural Hazards and Disaster Science (CNDS), Villavägen 16, Uppsala, 752 36, Sweden

ARTICLE INFO

Keywords:
Design load
Wave tank experiment
WEC-Sim
Bayesian
Markov chain Monte-Carlo
Long-term extreme response
Short-term extreme response
Probabilistic failure

ABSTRACT

To ensure a reliable operation over the life time of wave energy converters (WECs), a number of load cases need to be considered according to international standards for marine structures to determine an optimal design. This paper outlines the procedure of obtaining an environmental design load for the line force of a 1:30 scaled point-absorber WEC using an environmental contour with a 50-year return period for the Dowsing site in the North Sea. To obtain the response of the WEC during extreme conditions, a numerical WEC-Sim model is developed and calibrated with experimental wave tank tests to augment the data required for such design load analysis. The design load for the line force is estimated based on the full long-term extreme response computed from the full sea state approach by considering 180, 360, and 720 sea state samples as well as the contour approach for the sea state that gives the most extreme response. Further, a probabilistic approach is used to quantify the probability of failure for a critical mechanical component of the system such as shackle. The result shows that the numerical WEC-Sim model is able to sufficiently replicate the real response of the system during extreme irregular waves. The Bayesian theory with Monte-Carlo algorithm is found to be an excellent tool for identifying the degree of belief in the statistical models used for the short-term extreme response analysis. Considering the ultimate limit state, the design load for the 1:30 scaled system is calculated as 670.95 N (i.e. 18.11 MN for a full-scale system) after applying the partial load safety factor of 1.35 on the full long-term extreme response of the system for the 9.1 years return period (i.e. 50 years in a full-scale model).

1. Introduction

To assess the survivability of marine structures, the design load cases (DLCs) are required to be determined for the highest expected loads over the life time of a device. There are a few international standards for marine structures (DNV, 2014; IEC, 2016; Commission et al., 2019) outlining the best practices to determine the design load cases. The international standards recommend to obtain the design load for each load type (i.e. hydrostatic, hydrodynamics, and aerodynamic loads) and environmental load conditions (i.e. normal, survival under extreme, and abnormal environmental conditions). The 50-year sea states characterized by significant wave height (H_s) and peak period (T_p) are advocated by the International Electrotechnical Commission (IEC) to model the extreme wave conditions and the response of the wave energy converters (WECs) during their survival mode (Neary et al., 2021).

The question of finding the best framework to define the design load for offshore structures is addressed by many authors by looking through different aspects such as data augmentation, environmental contour methods, short-term and long-term extreme response methods, and more. van Rij et al. (2019a) approximated the design load for a two-body point-absorber (RM3) considering three different computational fidelity: a potential flow boundary-element method (WAMIT) in the frequency domain, a modified version of the linear-based WEC-Sim model in the time domain, and a computational fluid dynamics (CFD) model coupled with the finite element method (FEM) in time domain for both focused and regular waves. Through comparison of the numerical data with the experimental, the authors found that: WAMIT could not

☆ This research is supported by the Swedish Energy Agency (project number 47264-1), the Swedish Research Council (grant number 2020-03634), and StandUp for Energy, Sweden. Erik Nilsson was funded partly by the Swedish Research Council FORMAS (Grant No. 2018-01784) and the Centre of Natural Hazards and Disaster Science (CNDS), Sweden.

* Corresponding author.
E-mail address: zahra.shahroozi@angstrom.uu.se (Z. Shahroozi).

https://doi.org/10.1016/j.apor.2022.103305
Received 29 March 2022; Received in revised form 22 July 2022; Accepted 29 July 2022
Available online 10 September 2022

accurately capture the nonlinear mooring force, the three-dimensional structural moments were underestimated by their WEC-Sim model, and high nonlinear responses were achieved by CFD coupled with FEM to predict the linear-based most-likely extreme response (MLER) design load for the focused waves. Edwards and Coe (2019) evaluated five environmental contours, i.e. principal component analysis (PCA), Rosenblatt, Gaussian, Gumbel, and Clayton, for the two-body floater RM3 WEC. They observed that the PCA method predicted larger significant wave height for longer energy periods considering the given data set. The authors further noted the importance of this finding and its influence on the design decisions when assessing for instance mooring tension that is a low frequency phenomenon. Neary et al. (2020) compared different data sources (i.e. buoy measurements and wave model outputs), and different methods (i.e. univariate and bivariate) to estimate extreme sea states for several regions along the US East and West Coasts. They concluded that for the same data, both univariate and bivariate methods showed fair agreement on average with mostly random discrepancies. When comparing the extreme significant wave heights derived from two data sources, they detected a systematic bias for which a simple linear correction could compensate for those from buoy measurements, while such an approach was found insufficient for those from the environmental contour. Vanem (2015) investigated the uncertainty associated to the estimation of the extreme values for three data sets for the North Atlantic Ocean. The summary of the estimated 20-year and 100-year return values for various methods such as GEV, Gumbel, Weibull, Frechet, GPD, and the average conditional exceedance rate method (ACER) were presented. A large variability was noticed depending on the extreme value analysis approach. Further, the author inferred that it is not straightforward to select a single method or approach that is entirely preferred for this sort of analysis. Coe et al. (2018b) inspected the best-practice for predicting the design response of a spheroid floater WEC using full sea state long-term approach. Evidence showed that 50 sea states within the environmental contour provided a stable result for the given WEC. Also, increasing the number of sea states did not change the predicted response level notably, however, it reduced the uncertainty in the response level.

The main objective of this study is to determine the design load for the line force of a point-absorber WEC from an environmental contour with 50-year return period for the Dowsing Site in the North Sea. The novelties of the paper are to present: (1) a numerical WEC-Sim model with inclusion of different friction sources that is calibrated for extreme conditions based on the wave tank experimental data; (2) a statistical approach based on the Bayesian theory and Markov chain Monte-Carlo algorithm as a guideline to find the best model for the short-term extreme response; (3) the design load for the line force and the discussion on the probability of failure for a critical component of the system based on a wave tank experiment performed for extreme wave conditions.

The remainder of the paper is organized as follows: in Section 2, the experimental wave tank setup, numerical WEC-Sim model, and calibration for data augmentation are explained. Further, the theory and method to determine the design load through short- and long-term extreme analyses and the probabilistic failure using reliability analysis are explicated. The results of the WEC-Sim model, statistical approaches for computing the short- and long-term extreme response of the system, and the probabilistic failure analysis of a critical component are presented in Section 3. The discussion of the results, the uncertainties in the methods, and the possible future works are deliberated in Section 4. Lastly, Section 5 summarizes the conclusion of the work.

2. Theory and method

2.1. Design load case strategy

The design load case is defined as a design situation during which different loads are exerted on the structure. The design situations may consist of: power production; start-up; normal shutdown; emergency shut down; parked or idling; transport, maintenance, and repair. The strategy to define the environmental design load (DL) for the line force of a point-absorber WEC in this study is summarized as: First the environmental condition is obtained by Wrang et al. (2021) for a 50-year environmental contour for the Dowsing site. Second, the physical 1:30 scaled wave tank experiment is conducted by Shahroozi et al. (2022) where the sea states are chosen based on the 50-year environmental contour obtained by Wrang et al. (2021). Third, the WEC-Sim (Ruehl et al., 2021) numerical dynamic model is constructed and validated against experimental data for further data augmentation. Some information about the WEC-Sim model is given in Shahroozi et al. (2021) and greater details are provided here. In this study, the simulation time of 1 h with 20 seeds (i.e. the same as DNVGL, 2015) is used. Fourth, the short-term extreme response for the 1-hour simulations is estimated through different statistical methods. Fifth, the long-term extreme response of the point-absorber WEC considered in this study is achieved for the Dowsing site in the North Sea. Sixth, the design load is specified by considering the partial safety factor for the load.

A limit state refers to a condition beyond which the structure and structural components fail to fulfill their design requirements (DNVGL, 2015). The limit states may be divided into different categories such as (1) ultimate limit state (ULS) that is associated to the maximum capacity (resistance) of the load-carrying device and its subsystems; (2) fatigue limit state (FLS) that corresponds to the failure of the system resulted form cyclic loading; (3) accidental limit state (ALS) that is related to the survival conditions after a damage or due to nonlinear environmental conditions; (4) serviceability limit state (SLS) that refers to tolerance criteria for the design usage purpose (DNVGL, 2015). Depending on the operational condition, the design load cases need to be considered for different limit states, i.e. ULS, FLS, ALS, and SLS, and considering different load categories, i.e. permanent load, variable functional load, environmental load, and deformation load. Here, we focus on the ultimate limit state to identify the design load for the line force based on the environmental loads.

Note that the computation for both short-term and long-term extreme response analyses is conducted for the 1:30 scaled system. Therefore, when considering 20 seeds of 1 h simulation time for a full-scale model, it corresponds to 20 seeds of 0.18 h for a 1:30 scaled model. In this study, the Froude scaling law is used to translate the parameters between the full-scale and 1:30 scaled models.

2.2. Environmental contour and sea states

The best practices from international standards and various modern design codes recommend to adapt the short-term environmental conditions on the basis of the environmental contour using inverse first-order reliability method (I-FORM) and the joint probability distribution of the short-term environmental parameters to identify the sea states around or inside the environmental contour with a certain return period. Later, this identification of the short-term conditions will be used to calculate the long-term extreme response of the system.

Here, the sea states are selected based on a 50-year environmental contour using the I-FORM hybrid method for the Dowsing site situated at 56 km from the west coast of the United Kingdom in the North Sea, see Fig. 1. The focus of the analyses here is solely on irregular wave representations, i.e. generated based on the JONSWAP spectrum (Veritas, 2010). Along the contour line, only sea states 5a to 10, excluding sea state 7 are tested in the wave tank experiment, see Table 1. Sea state 7 was not experimentally tested due to the limitations of the wavemaker in the wave tank of the Ocean and Coastal Engineering Laboratory of Aalborg University to generate such an extreme sea state. The reader is encouraged to refer to Shahroozi et al. (2022) to further read about the extremity of the selected sea states and the hydrodynamic nonlinearities they lead to.

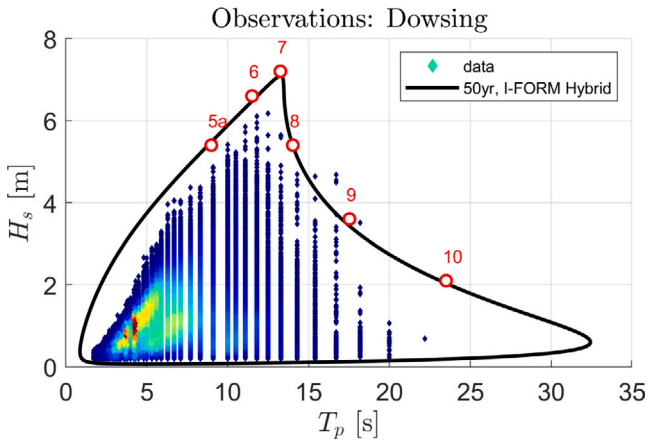

Fig. 1. The environmental contour for sea states with the 50-year return period for the Dowsing site in the North Sea is illustrated for the full-scale system. X and Y axes represent the peak period (T_p) and significant wave height (H_s), respectively. In this paper, sea states 5a, 6, 7, 8, 9, 10 around the environmental contour using I-FORM hybrid are studied for the contour approach. Applying the Froude-scaling law, 1:30 scaled sea states are acquired as the inputs to both experimental and numerical investigations.
Source: Adapted from Katsidoniotaki et al. (2021)

Table 1
Sea state information for the 1:30 scaled model based on Fig. 1.

Sea states	5a	6	7	8	9	10
H_s [m]	0.18	0.22	0.24	0.18	0.12	0.07
T_p [s]	1.64	2.10	2.42	2.56	3.20	4.29

In Wrang et al. (2021), different methods for construction of the environmental contour such as standard and hybrid I-FORM, modified version of principle component analysis (PCA), and 2-dimensional peaks-over-threshold (2D POT) were described for four study sites, one of which was the Dowsing site in the North Sea considering both observation and hindcast model data. The authors found that the PCA method did not properly improve the dependency for the given data unlike the PCA application explained in Eckert-Gallup et al. (2016), and the 2D-POT method underestimated the extreme sea states. However, the I-FORM hybrid method with a slight modification provided superior fit in comparison.

The outline of the I-FORM hybrid method that was previously described in Wrang et al. (2021) is summarized here: Assuming the short-term extreme sea states, i.e. characterized by the significant wave height (H_s) and energy period (T_p), are well-known, a joint probability density function (PDF) can be utilized to determine the long-term extreme sea states as (Haver, 1986, 2002; Haver and Winterstein, 2008; Ronold et al., 2010; Berg, 2011):

$$p_{H_s,T_p}(h_s,t_p) = p_{H_s}(h_s)p_{T_p|H_s}(t_p|h_s) \tag{1}$$

where h_s and t_p refer to certain values of H_s and T_p. Note, that in Eq. (1), the consideration of either zero-crossing period (T_z), energy period (T_e), or peak period (T_p) is valid. The procedure to compute Eq. (1) can be broken down into the following steps:

i. Calculate the marginal probability density function of H_s through the hybrid model (Haver, 1986) as:

$$p_{H_s}(h_s) = \begin{cases} \frac{1}{\sqrt{2\pi}\tilde{b}h_s}\exp\left\{-\frac{(\ln h_s-\tilde{a})^2}{2\tilde{b}^2}\right\}, & \text{for } h_s \le \eta \\ \frac{\tilde{d}}{\tilde{c}}\left(\frac{h_s}{\tilde{c}}\right)^{\tilde{d}-1}\exp\left\{-\left(\frac{h_s}{\tilde{c}}\right)^{\tilde{d}}\right\}, & \text{for } h_s > \eta \end{cases} \tag{2}$$

where η is called the threshold or transition point. First, a log-normal distribution is fitted to all observations of H_s for $h_s \le \eta$. The parameters $\tilde{a}$ and $\tilde{b}$ identify the mean and variance of the variable $\ln h_s$, respectively. Then, the shape, $\tilde{d}$, and scale, $\tilde{c}$, parameters of the Weibull tail distribution are achieved through continuity requirement of the hybrid model in both density and distribution functions at $h_s = \eta$. It is important to achieve an appropriate fit for the most extreme values of H_s, therefore, Wrang et al. (2021) considered only the upper 10% of the H_s data to determine the threshold, η. The authors noted that the Cramér–von Mises goodness-of-fit (GOF) metric is used to define the value of η through considering only this upper 10% of the H_s data.

ii. Calculate the marginal probability density function of T_p conditioned on H_s using a log-normal model as (Haver and Winterstein, 2008; Berg, 2011):

$$p_{T_p|H_s}(t_p|h_s) = \frac{1}{\sqrt{2\pi}\sigma(h_s)t_p}\exp\left\{-\frac{(\ln t_p - \mu(h_s))^2}{2\sigma(h_s)^2}\right\} \tag{3}$$

where $\sigma(h_s)$ and $\mu(h_s)$ denote the conditional standard deviation and expected value of the variable $\ln t_p$ given h_s, respectively. A smoothed function is used on parameters $\sigma(h_s)$ and $\mu(h_s)$ to extrapolate the data beyond the observation range, i.e. the same as Eq. (7) and Eq. (8) in Haver and Winterstein (2008):

$$\begin{aligned} \mu(h_s) &= a_0 + a_1 h_s^{a_2} \\ \sigma(h_s)^2 &= b_0 + b_1\exp\{-b_2 h_s\}. \end{aligned} \tag{4}$$

One way to obtain the parameters a_0, a_1, a_2, b_0, b_1, and b_2 is to split the H_s data into bins, fit a log-normal distribution to T_p data in each bin to obtain $\mu(h_s)$ and $\sigma(h_s)$, and finally estimate these parameters by curve fitting to the calculated $\mu(h_s)$ and $\sigma(h_s)$ for various h_s.

iii. Transform the cumulative distribution functions (CDF) into a u-space of uncorrelated standard Gaussian variables, U_1 and U_2, using the Rosenblatt transformation scheme (Rosenblatt, 1952; Chang, 2015):

$$\begin{aligned} P_{H_s}(h_s) &= \Phi(u_1) \\ P_{T_p|H_s}(t_p|h_s) &= \Phi(u_2) \end{aligned} \tag{5}$$

where $\Phi()$ is defined as the standard Gaussian cumulative distribution function. This transformation removes the correlation between H_s and T_p.

iv. Define the 50-year contour line in the u-space along the circle $\beta = \sqrt{U_1^2 + U_2^2}$ where β is the radius of the circle and can be obtained as (Berg, 2011):

$$\beta = \Phi^{-1}\left(1 - \frac{T_{ss}}{8760\,T_r}\right) \tag{6}$$

where T_{ss} and T_r are the sea state duration and return period, respectively. The environmental contour here is constructed based on the sea state duration (T_{ss}) of one hour. It used to be a common practice to *inflate* the circle to achieve a satisfactory environmental contour by compensating for the approximation of *the true stochastic response with its median value* (Berg, 2011): $\beta^* = \beta/\sqrt{1-\alpha^2}$ where α^2 is usually given in the range of 0.1 to 0.2. Now, other alternatives may be used to obtain more accurate environmental contour such as correcting the median response or considering a higher percentile of H_s data to define the threshold value as it was considered for the hybrid model in Wrang et al. (2021) and explained in Eq. (2). Hence, no inflation rate was taken in the hybrid model by Wrang et al. (2021) which is used here.

v. Transfer back the standard Gaussian variables, U_1 and U_2, into H_s and T_p to construct the 50-year environmental contour based on the original coordinates:

$$\begin{aligned} h_s &= P_{H_s}^{-1}(\Phi(u_1)) \\ t_p &= P_{T_p|H_s}^{-1}(\Phi(u_2)|H_s = h_s). \end{aligned} \tag{7}$$

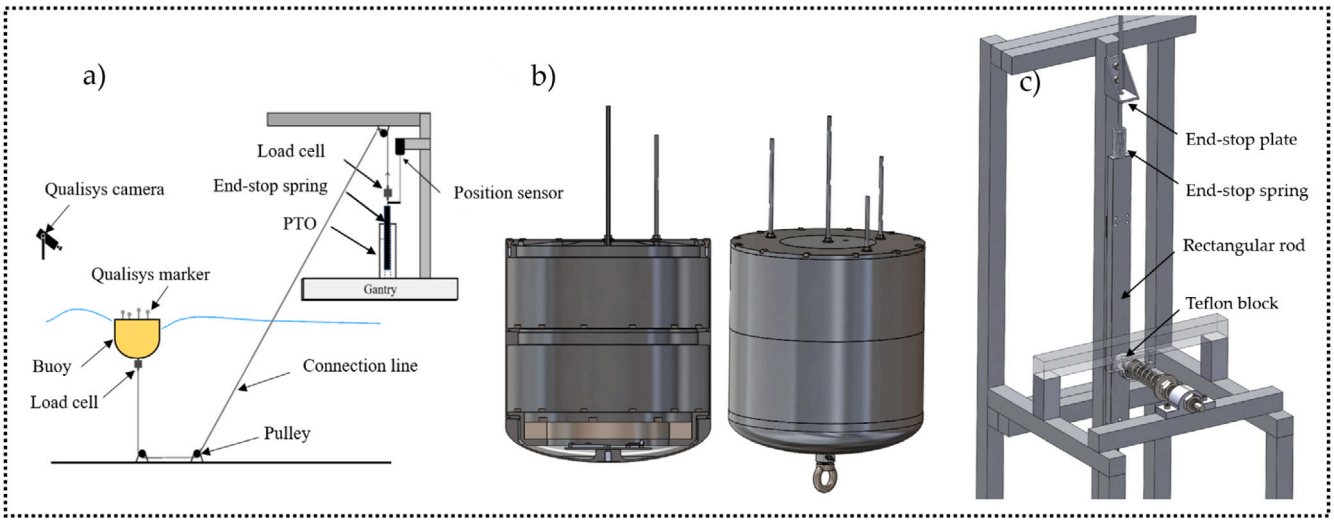

Fig. 2. In (a), the wave tank sketch is shown. In (b), the section view and 3D view of the buoy is illustrated. In (c), the linear friction PTO is depicted. *Source:* The sketches (a) and (b) are retrieved from Shahroozi (2021), Shahroozi et al. (2021), respectively.

The data to draw the environmental contour is based on 15.4 years of observations between 2003 and 2019 with a network of wave buoy measurements (WaveNet, 2022) located at the UK coastline (Wrang et al., 2021). Note that the observational data set of 15.4 years can be relatively short to construct a 50-year environmental contour. Often in extreme value analysis (e.g. generalized extreme value model (GEV) fit using annual maxima), it is more common to derive return levels corresponding to about twice the length of the available record. However, there are very few observational sites that have about 25 years of observations, and wave-modeled data sets often do not reproduce all aspects of observations well enough to act as a substitute for the direct observations.

2.3. Wave tank experiment

The small scale 1:30 wave tank experiment is conducted for extreme wave conditions in the Ocean and Coastal Engineering Laboratory of Aalborg University. The experimental setup consists of a linear friction power take-off (PTO), an aluminum cylindrical buoy with ellipsoidal bottom, and three pulleys which connect the buoy to the PTO via a 3 mm Dyneema rope, see Fig. 2. The wave tank experimental setup here is a 1:30 scaled of the Uppsala University WEC. This scaling is chosen to be large enough to represent a realistic system while being small enough so that the extreme wave from the North Sea can be generated in the wave tank test (Shahroozi et al., 2022).

The PTO applies a constant friction damping force in the vertical movement of the rod that is rubbing against a spring-Teflon module. The total PTO mass is 2.138 ± 0.001 kg including the translator and all its attached equipment. In this study, we only focus on the PTO damping force of 7.4 N, i.e. corresponding to the damping configuration D_1 in Shahroozi et al. (2022). The motion of the translator is constrained only with an upper end-stop with a spring coefficient of 5.9 N/mm. The stroke length is considered 220 mm.

The buoy has a diameter, height, and draft of 330 mm, 380 mm, and 230 mm, respectively, with a mass of 15.73 ± 0.001 kg. To minimize the drag forces, an ellipsoidal bottom is considered in the design of the buoy. The center of gravity is located at 118.6 mm directly above the bottom center of the buoy. Considering a coordinate system at the center of gravity with the Z axis pointing in the upright vertical direction, the moments of inertia, i.e. I_{xx}, I_{yy}, and I_{zz}, are 0.3537 kg m^2, 0.3536 kg m^2, and 0.2918 kg m^2, respectively. SolidWorks (CAD) is used to compute both center of gravity and moments of inertia.

The measurement system is comprised of: a draw-wire position sensor to measure the translator movement, a Qualisys system to track the motion of the buoy in six degrees of freedom using four cameras, two load cells to collect the force data with a capacity of 2000 N and accuracy of ± 0.3%, and eight wave gauges to measure the surface elevation. The data from the draw-wire position sensor and load cells are logged and transmitted with two SG-Link-200-OEM which communicate with one LORD sensing WSDA with the same sampling frequency as wave gauges, i.e. 256 Hz, while the Qualisys system has a sampling frequency of 300 Hz. The buoy is positioned at 6.54 m and 6.477 m from side walls, and 4.819 m from the wavemaker. The water depth of 0.73 ± 0.02 m is considered. The detailed information about the wave tank experiment can be found in Shahroozi et al. (2022) and Shahroozi et al. (2021).

2.4. WEC-Sim model

The WEC-Sim (Ruehl et al., 2021) model consists of a buoy that is meshed by the Rhino software (Rhinoceros, 2021) and three one-degree-of-freedom (1-DoF) WEC-Sim PTOs connected in series to mimic the motion of the buoy in surge, heave, and pitch motion. To emphasize, the physical PTO in the experiment is a linear friction PTO that is moving only in the vertical direction (1-DoF), while, the three PTOs in the WEC-Sim model are merely simulation blocks which both constrain the motion of the buoy in three degrees of freedom, and provide the feedback and actuation force, see Fig. 3.

The WEC-Sim simulation has been considered for 1-hour storms with 20 seeds corresponding to 0.18-hour duration for the 1:30 scaled model. This simulation length is chosen based on the 1-hour sea state duration in the construction of the environmental contour, see Eq. (6).

2.4.1. Weakly nonlinear effects

To capture weakly nonlinear effects in the buoy's dynamic, the nonlinear buoyancy and Froude–Krylov forces (Lawson et al., 2014) are considered using *nlHydro = 2* in the WEC-Sim input file. This option computes the Froude–Krylov and nonlinear hydrostatic forces through the integration of the pressure owing to the instantaneous wave elevation and instantaneous buoy position. Thereby, the buoyancy is no longer assumed as a constant value, and in general, the equation of motion is approximated with a higher accuracy.

2.4.2. Drag coefficients and force

The quadratic viscous drag force is computed as $\mathbf{F}_D = -F_D\hat{v}$ in vector form where F_D is the magnitude of the drag force, and $\hat{v}$ is the unit vector in the direction of velocity. This implies that the

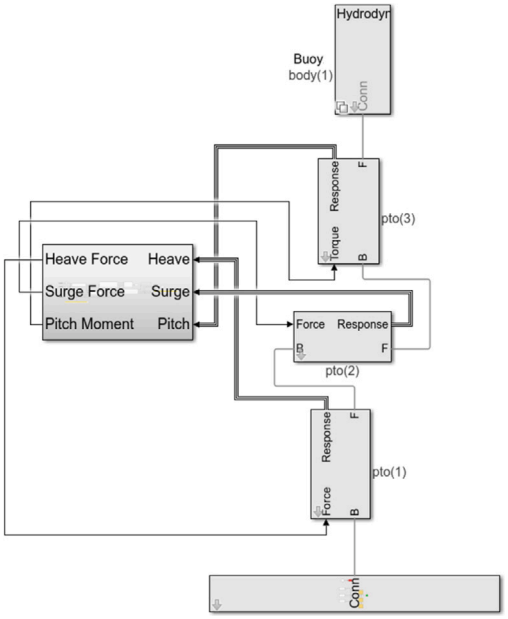

Fig. 3. The WEC-Sim model showing the buoy and the three WEC-Sim PTOs connected in series.
Source: Retrieved from Shahroozi et al. (2021)

drag force opposes the velocity of the buoy at all times. Further, the magnitude of the drag force is given as $F_D = 1/2\rho A C_D v^2$ in which ρ is the water density, A is the cross-sectional area of the buoy, and v is the buoy's velocity. The derivation of the viscous drag coefficient C_D can be achieved either through numerical simulations (Todalshaug et al., 2011; van Rij et al., 2017, 2019b), following the Reynolds number and the device geometry (Tosdevin et al., 2020), or with some experimental measurements (Bosma et al., 2016). The experimental measurement technique uses the decay test to obtain C_D in several degrees of freedom. However, it is not straightforward to perform the decay test in all degrees of freedom. In this study, the decay test is experimentally performed only for the heave motion. Then, the drag coefficient in heave is acquired through curve fitting of the decay test response from experiment to the numerical (WEC-Sim) one by means of least square method. The drag coefficient in surge is achieved through tuning the amplitude response operator (RAO) in WEC-Sim to the experimental one. The derivation of the drag coefficient in pitch motion is somewhat more difficult and the experimental measurement (i.e. performing the decay test in pitch motion) is more crucial to accurately calculate this coefficient in pitch motion. Here, in the absence of decay test in pitch motion, an alternative, but by no means the best, solution is considered where the least square method is used to calibrate the response of the buoy in pitch motion to the experimental one that is captured by the Qualisys system, in a regular sea state. Hence, the drag coefficient and characteristic area corresponding to the surge, heave, and pitch are introduced using *body(1).viscDrag.cd* and *body(1).viscDrag.characteristicArea* in the WEC-Sim input file, respectively. Note that the WEC-Sim model implemented in this study is more advanced and complex in comparison with the preliminary model explained in Shahroozi et al. (2021) through consideration of a more accurate way to simulate the end-stop spring and pulley friction modules. Hereupon, the input parameters for the drag coefficient are updated to 0.21, 0.21, and 0.01 for surge, heave, and pitch respectively.

2.4.3. WEC-Sim line force

The line force in the WEC-Sim model is determined through defining the forces in the heave and surge motion, and the moment in pitch motion. First, a body-fixed coordinate system (i.e. WEC-Sim PTOs' tracker)

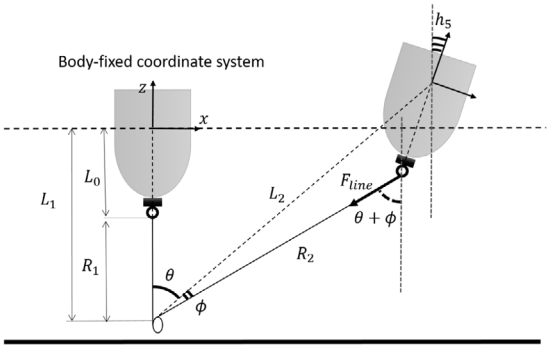

Fig. 4. Buoy's motion trajectory to derive the forces in heave and surge motion, and the moment in pitch motion.
Source: Retrieved from Shahroozi et al. (2021).

is considered. This coordinate coincides with the global coordinate system located at the water plane when the waves are undisturbed. Then, given the free body diagram that is shown in Fig. 4, the forces and moment for the *buoy* can be derived as:

$$\begin{aligned} F_{\text{surge}} &= -F_{\text{line}} \sin(\theta + \phi) \\ F_{\text{heave}} &= -F_{\text{line}} \cos(\theta + \phi) \\ M_{\text{pitch}} &= -F_{\text{surge}} L_0 \cos(h_5) + F_{\text{heave}} L_0 \sin(h_5) \end{aligned} \tag{8}$$

where the forces in heave and surge motion are F_{heave} and F_{surge}, respectively, while the moment in pitch motion is defined as M_{pitch}. Further, F_{line} is the line force seen from the buoy side. Looking at Fig. 4 again, the distance from the water plane to the loop connected to the buoy is defined as L_0. Moreover, h_5 is the pitch angle of the buoy, and θ is the angle between the equilibrium position of the buoy and its disturbed position considering the body-fixed coordinate system. Further, ϕ is the angle between L_2 and R_2. Hence, the angles θ and ϕ are obtained as (Shahroozi et al., 2021):

$$\begin{aligned} \theta &= \tan^{-1}\left(\frac{h_1}{L_1 + h3}\right) \\ \phi &= \sin^{-1}\left(\frac{L_0 \sin(\theta - h_5)}{R_2}\right) \end{aligned} \tag{9}$$

where the surge and heave displacements are defined by h_1 and h_3, respectively, and L_1 is the distance from the pulley at the basin to the water plane. The distance between the pulley connected at the wave basin to the load cell connected at the bottom of the buoy at its non-equilibrium position is R_2 and is computed as (Shahroozi et al., 2021):

$$R_2^2 = L_2^2 + L_0^2 - 2L_0 L_2 \cos(\theta - h_5) \tag{10}$$

where $L_2 = h_1^2 + (L_1 + h_3)^2$ is the distance form the body-fixed coordinate system of the buoy at non-equilibrium position to the pulley connected at the basin.

Looking at the PTO from the buoy side, the line force can be derived from the equation of motion (vector form) as:

$$m_{\text{PTO}} \ddot{\mathbf{z}}_{\text{PTO}} = \mathbf{F}_{\text{line}} + \mathbf{F}_{\text{endstop}} + \mathbf{F}_{f_{\text{PTO}}} + \mathbf{F}_{fp} + m_{\text{PTO}} \mathbf{g} \tag{11}$$

where the translator mass including all the components connected to it is m_{PTO}, and $\mathbf{F}_{\text{endstop}}$, $\mathbf{F}_{f_{\text{PTO}}}$, and $\mathbf{F}_{fp}$ are the end-stop spring, PTO, and pulley friction forces, respectively. Lastly, $\ddot{\mathbf{z}}_{\text{PTO}}$ and $\mathbf{g}$ are the PTO and gravitational accelerations, respectively.

2.4.4. WEC-Sim PTO friction model

Modeling a friction system to mimic the physical system accurately is not a trivial task and rather involves large degrees of complexity. Here, a concise explanation of various static and dynamical friction models are presented. Thereafter, the choice of the friction model for

the WEC-Sim system considered here is described. The readers are encouraged to refer to Huang et al. (2019) for further information, where the authors provided an excellent overview of different friction models and compensation schemes.

A classical static friction model is one of the simplest and most well-known models that is featured by its relation between the velocity and frictional force, representing the Stribeck effect in friction (Armstrong-Helouvry and Soom, 1992; Armstrong-Helouvry, 2012), and also includes the Coulomb and viscous frictions. In this model and in the absence of viscous friction, when two objects are slipping against each other, the frictional force stays constant until the direction of motion is reversed (Fu et al., 2017; Tjahjowidodo et al., 2007). Then after, it has been discovered experimentally that there is a memory effect owing to the switch over from one state to another. Thereby another static friction model called time-delay (Hess and Soom, 1990) is introduced to capture this memory effect by considering a time lag. The challenge with this model is that a large amount of experimental data should be available to build up the model. Later, through a set of observations, it has been realized that although the classical and time-delay models represent the sliding phase, they do not reflect the friction at very low velocities existing in the microscopic level, e.g. deformation of surface asperities. Therefore, a dynamical friction named LuGre model (De Wit et al., 1995) has been proposed to both account for slip and stick motion as well as zero-slip displacement. However, the LuGre Model is not able to capture pre-sliding hysteresis behavior properly. The elasto-force is added in the LuGre model to resolve this drawback. Hence, the result of this correction is called the Generalized Maxwell-slip (GMS) model, i.e. a dynamical friction model (Swevers et al., 2000; Lampaert et al., 2002).

Although the more advanced models can replicate the physical behavior more accurately, more parameters are often required to be estimated, and they are computationally more expensive. Therefore, one must consider these when choosing between simple and advanced models especially when the computational time is important.

In this work, the PTO friction is found to be best represented by a static friction model considering the Stribeck, and Coulomb components due to first and foremost: the necessity of high-speed simulation runs for calculating the WEC response for different sea states, and second, the absence of the experimental data for derivation of other friction model parameters. The friction force in this study is modeled as a function of the relative velocity (Armstrong and de Wit, 1995) as:

$$F_{f_{\mathrm{PTO}}} = \sqrt{2e}(F_{\mathrm{brk}} - F_C)\exp\left(-\left(\frac{\dot{z}_{\mathrm{PTO}}}{v_{\mathrm{St}}}\right)^2\right)\frac{\dot{z}_{\mathrm{PTO}}}{v_{\mathrm{St}}} + F_C\tanh\left(\frac{\dot{z}_{\mathrm{PTO}}}{v_{\mathrm{Coul}}}\right) \tag{12}$$

where the breakaway friction and Coulomb forces are denoted as F_{brk} and F_C, respectively. Further, the Stribeck velocity threshold is defined as $v_{\mathrm{St}} = v_{\mathrm{brk}}\sqrt{2}$, and the Coulomb velocity threshold is identified as $v_{\mathrm{Coul}} = v_{\mathrm{brk}}/10$ where v_{brk} is the breakaway friction velocity. The relative velocity is identified as $\dot{z}_{\mathrm{PTO}}$. Moreover, e is the Euler's number that is equal to 2.71828 approximately. Note that the viscous friction is considered zero due to a dry contact between the surfaces (i.e. here between Teflon and aluminum rod). To put the concept in perspective, Fig. 5 illustrates the contribution of each frictional component, where the sum of the Stribeck and Coulomb frictions at zero velocity presents the breakaway friction force. The Coulomb friction is the friction that occurs as a constant force by opposing the movement. The Stribeck friction refers to the characteristic of the negative slope that occurs at low velocities.

2.4.5. WEC-Sim pulley friction model

Similarly, the pulley friction is modeled as a function of the relative velocity:

$$F_{fp} = \mu_p F_{\mathrm{line}}\tanh\left(\frac{\dot{z}_{\mathrm{PTO}}}{v_{\mathrm{Coul}}}\right) \tag{13}$$

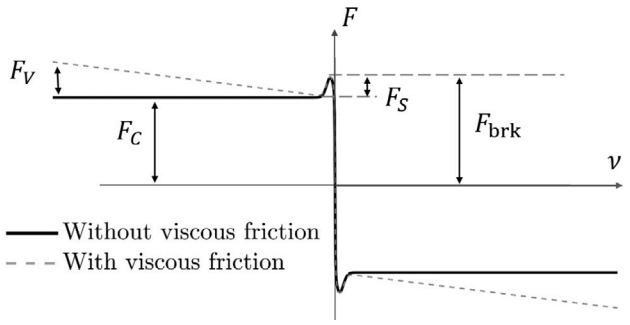

Fig. 5. The contributions of the Stribeck, Coulomb, and viscous components for the friction model that is adopted to simulate the WEC-Sim PTO friction.

where μ_p is the pulley friction coefficient. This coefficient is obtained through a set of simple experiments where the translator is manually moved downward with nearly constant velocity while measuring the forces induced on the load cells from both PTO and buoy sides. The pulley friction for such a quasi-static motion when the rope is in tension is obtained by subtracting the forces gathered by the load cells attached to the buoy and PTO translator. Then, the pulley friction coefficient can be computed by considering the proportionality of the friction force to the line force that is seen from the buoy side (measured by the buoy load cell). Afterwards, $\tanh(\dot{z}_{\mathrm{PTO}}/v_{\mathrm{Coul}})$ relates this friction to the relative velocity. For the sake of simplicity, we neglect the effect of the Stribeck friction as it has a minimal effect. Thereby, we only model the Coulomb component where the Coulomb force in Eq. (12) is $F_C = \mu_p F_{\mathrm{line}}$. Note that the pulley friction introduced here is a closed loop module in WEC-Sim due to its dependency to F_{line}.

2.4.6. WEC-Sim end-stop module

The end-stop mechanism protects the structure from extreme motions and impact forces during extreme wave conditions, and therefore, it reduces the mechanical failure to a great degree (Chen et al., 2021; Eskilsson et al., 2021). For the experiment conducted for this study, a spring with a coefficient of 5.9 N/mm is used for the end-stop so that the experiment can replicate the extreme wave conditions where the full compression of the end-stop spring is often observed. The readers are encouraged to see Fig. 22 and section 4.4 in Shahroozi et al. (2022) to have a further insight about the end-stop spring mechanism and compression in extreme sea states. Thus, the involvement of the end-stop spring leads to strong non-linearities which has a dominant effect in the equation of motion.

It is common to model this module as a rigid or an elastic end-stop. In the rigid end-stop, the momentum conservation theorem holds, and the contact stop tries to replicate an ideal impact where an instantaneous change in the velocity occurs. It is not straightforward to model a rigid end-stop in WEC-Sim since it results in an instantaneous infinite force and acceleration in the system. On the other hand, the elastic end-stop gives closer results to the actual behavior of the system where the contact stop is often modeled as a spring-damper. In this study, the end-stop is modeled as an elastic end-stop following:

$$F_{\mathrm{endstop}} = \begin{cases} k_{\mathrm{es}}(l_0 - l_c) + k_{\mathrm{st}}\left(z - \frac{l_s}{2}\right) + c_{\mathrm{st}}\dot{z}, & (i) \\ k_{\mathrm{es}}(l_0 - l_c) + k_{\mathrm{st}}\left(z - \frac{l_s}{2}\right), & (ii) \\ k_{\mathrm{es}}\left(z - \left(\frac{l_s}{2} - (l_0 - l_c)\right)\right), & (iii) \end{cases} \tag{14}$$

where (i) is when $z > l_s/2$, and $\dot{z} > 0$, (ii) is for $z > l_s/2$, and $\dot{z} \le 0$, and (iii) is for $l_s/2 - (l_0 - l_c) < z \le l_s/2$. Here, the end-stop spring coefficient is k_{es}, and k_{st} is the equivalent spring coefficient of the structure. The stroke length is denoted as l_s, and the initial and compressed lengths of the end-stop spring are l_0 and l_c, respectively. The energy dissipation due to the impact after full spring compression

is modeled as a viscous damper with the coefficient c_{st} acting only when the PTO is compressing the end-stop, i.e. $\dot{z} > 0$.

2.5. Short-term extreme response analysis

The short-term extreme response gives the answer to what will be the largest response of the device (e.g. the bending moment, or mooring line force) for a device operating in a particular sea state for a specific time, i.e. usually equivalent to 1 to 3 h storm duration, and it is assumed that during this time, the spectral density function of the sea state remains constant (Michelen and Coe, 2015; Coe et al., 2018b).

The typical approaches to analyze the extreme value data are block-maxima and peaks-over-threshold. In the block-maxima method, the data is blocked into non-overlapping blocks of equal length, and a generalized extreme value model (GEV) is used to be fitted to the maximum of each block (Coles et al., 2001). The GEV cumulative distribution function fitted to the maximum of each block is defined as:

$$P_{\mathrm{GEV}}(x) = \begin{cases} \exp\left(-\left(1+\frac{k(x-\mu)}{\alpha}\right)^{-\frac{1}{k}}\right), & k \neq 0 \\ \exp\left(-\exp\left(-\frac{(x-\mu)}{\alpha}\right)\right), & k = 0 \end{cases} \tag{15}$$

for $\{x : 1+k(x-\mu)/\alpha > 0\}$, $-\infty < \mu < \infty$, and $\alpha > 0$ where the location and scale parameters are introduced as μ and α, respectively. Further, the shape parameter is k. For $k = 0$, the distribution is called type I or Gumbel distribution, while for $k > 0$ and $k < 0$, the distribution is referred to as the Frechet distribution (type II) and reversed Weibull distribution (type III), respectively (Coles et al., 2001). Note that type III extreme value distribution is in fact the mirror image or reversed form of the Weibull distribution. On the other hand, the Frechet and non-reversed Weibull probability distribution functions are related with $p_{\mathrm{Frechet}}(x;k,\mu,\alpha) = -p_{\mathrm{Weibull}}(x;-k,\mu,\alpha)$. In the peaks-over-threshold method, a certain threshold is specified, and then a generalized Pareto distribution (GPD) model is fitted to the exceedances that correspond to the data above a chosen threshold less the threshold (u): $z = x - u$ for $x > u$ (Coles et al., 2001). The GPD cumulative distribution function fitted to the exceedances is given as:

$$P_{\mathrm{GPD}}(z) = \begin{cases} 1-\left(1+\frac{kz}{\alpha}\right)^{-\frac{1}{k}}, & k \neq 0, 1+\frac{kz}{\alpha} > 0 \\ 1-\exp\left(-\frac{z}{\alpha}\right), & k = 0, z > 0 \end{cases} \tag{16}$$

where the scale and shape parameters are denoted as α, and k, respectively. In the special case of $k = 0$, the distribution is reduced to the exponential distribution (ED). For $k < 0$, there is an upper bound of $u - \alpha/k$ for the distribution of exceedances, while for $k > 0$, the distribution has no upper limit (Coles et al., 2001).

Both block-maxima and peaks-over-threshold methods can be applied for both stationary, i.e. the data series has stochastic properties which are constant over time or unfollowed by strong variation patterns, and non-stationary sequences. The length of block size and the selected threshold should be considered with caution. Too low a threshold or block size leads to a bias in the model, whereas, too high of a threshold or block size results in a high variance. A pragmatic consideration of the block size of 1 year is often taken when dealing with the block-maxima method. This means that a large amount of data is required for statistical modeling via the block maxima method. A common practice to cope with the mutual dependency between exceedances in the peaks-over-threshold method is declustering, i.e. clustering the data through an empirical strategy, and therefore, fitting the GPD distribution to the maximum of each cluster. Hence, intermediate- to long-term data is desired to achieve an appropriate fit with the peaks-over-threshold method.

One important challenge from the reliability point of view in the design of WECs is to reliably identify the characteristic extreme value, i.e. corresponding to the most probable value (MPV) or to a specific fractile level of the short-term extreme distribution, for design checks given the low/intermediate amount of data (Sagrilo et al., 2011). There are several methods that can be applied to the low/intermediate time–history of non-Gaussian data to assess the short-term extreme value distribution. The simplest and most frequently used method is the Weibull tail-fit distribution where the Weibull probability distribution is fitted to the upper tail of the time-series peaks, and then, following an asymptotic assumption (Ang and Tang, 1984), the short-term extreme distribution can be achieved (Michelen and Coe, 2015). The Winterstein's method (Winterstein, 1988) is another well-established approach which utilizes a memory-less transformation to convert the standard Gaussian process according to the Hermite polynomials and the first four statistical moments of the time-series. Another fairly recent method is the average conditional exceedance rate (ACER) (Næss and Gaidai, 2009). This model provides more flexibility in comparison with the ones based on the asymptotic theory, and it considers the cascade of conditioning approximations with the first one defined by Markov-like approximation. Nevertheless, there is one limitation to this model: it can be considered only for the cases where the Gumbel distribution is considered as a proper asymptotic extreme value distribution. The aforementioned methods may typically be applied when a long-history of data is not available. However, the extreme response values are still subjected to some statistical uncertainties depending on the type of the data, the distribution model, and especially to the length of the simulation (Sagrilo et al., 2012). Sagrilo et al. (2011) suggested a straight-froward procedure to deal with uncertainties corresponding to the simulation length considering a single short-time simulation by introducing a safety factor that is adjusted to each extreme value method. In this study, the short-term extreme response analysis has been made considering the Weibull tail-fit, peaks-over-threshold, and two-parameter Weibull distributions that are explained in the following subsections. Note that the block-maxima analysis is the most straightforward method, however, as explained above and due to requiring a large amount of data, it has not been considered here.

2.5.1. Weibull tail-fit distribution

The Weibull tail-fit method (Sagrilo et al., 2002) is fitted to the upper tail of the parent distribution as it is the foremost important part in the computation of the extreme statistics (Ang and Tang, 1984). The following steps summarize the Weibull tail-fit approach:

i. Select the peaks of line force based on the zero up-crossings of the surface elevation. In other words, choose the peaks of forces in a time period between two consecutive zero up-crossings of the surface elevation.

ii. Compute an approximate cumulative distribution function of the peaks that are ordered in an ascending sequence (Sagrilo et al., 2002):

$$P(x_{P_i}) = \frac{i}{N+1} \tag{17}$$

where N is the total number of peaks, and i represents the ith order of peaks.

iii. Consider a set of limits for the CDF computed from the last step as $C_{\lim_j} = 0.6 + 0.05j$ for $j = 1, 2, \ldots, 7$ (Sagrilo et al., 2002). Then, for each CDF limit, fit a two-parameter Weibull distribution to the following data set: $(x_{P_i}, P(x_{P_i}))$ in which $P(x_{P_i}) > C_{\lim_j}$ (Sagrilo et al., 2011; Michelen and Coe, 2015). The cumulative distribution function of the two-parameter Weibull is considered as:

$$P_{\mathrm{Weibull}}(x_P) = 1 - \exp\left(-\left(\frac{x_P}{\alpha}\right)^k\right) \tag{18}$$

where α and k are the scale and shape parameters, respectively.

iv. Calculate the shape and scale parameters of the final Weibull distribution by taking the average of the estimated parameters (shape and scale) obtained for all $C_{\lim_j}$.

v. Compute the short-term extreme cumulative distribution function based on the cumulative distribution of the peaks as (Coe et al., 2016, 2018a; Michelen and Coe, 2015):

$$P_{st}(x) = P_P(x)^{N_{st}} \tag{19}$$

where the average number of peaks in each 1-hour short-term extreme simulation is $N_{st} = N(\Delta t_{st}/\Delta t)$, in which Δt_{st} is the 1-hour short-term extreme simulation period, and Δt is the total 20×1 hours simulation length. In more detail, let $x_{P_1}, x_{P_2}, \ldots, x_{P_{N_{st}}}$ be N_{st} number of independent peaks in the 1-hour short-term extreme period, then the probability of $x_{P_i} \leq x$ for $i = 1, 2, \ldots, N_{st}$ is $P_{st}(x) = \prod_{i=1}^{N_{st}} P_{P_i}(x)$.

2.5.2. Peaks-over-threshold distribution

The peaks-over-threshold method (Coles et al., 2001) is also employed to investigate the upper tail of the line force distribution. The outline of this method is presented through the following steps:

i. Specify the peaks of line force in the same way as explained in the first step (i.) of the Weibull tail-fit method in the previous subsection.
ii. Find an appropriate threshold for each sea state using the mean residual life plot as well as the shape and scale parameters stability plots, i.e. illustrated in Section 3. The classical technique to choose a proper threshold at which the generalized Pareto distribution gives a valid and suitable model is first to look at the mean residual plot from right to left and select the first point (threshold) that the mean residual curve follows an approximately linear trend. Then, for within the vicinity of the selected threshold, the shape parameter should be approximately constant, while the scale parameter should be linear (Coles et al., 2001).
iii. Fit the generalized Pareto distribution described in Eq. (16) to the exceedances of the peaks of the line force: $z_P = x_P - u$ for $x_P > u$.
iv. Calculate the cumulative distribution of peaks based on the cumulative distribution of exceedances through (Coe et al., 2016, 2018a; Michelen and Coe, 2015):

$$P_{P,\mathrm{GPD}}(z_P + u) = 1 - \left(\frac{N_{\mathrm{pot}}}{N} \left(1 - P_{\mathrm{GPD}}(z_P) \right) \right) \tag{20}$$

where N_{pot} is the number of peaks above the threshold, and N is the total number of peaks.
v. Compute the short-term extreme cumulative distribution function based on the cumulative distribution of the peaks in the same way as described in the last step Eq. (19) of the Weibull tail-fit method.

2.5.3. Bayesian theorem and Markov chain Monte-Carlo algorithm

The Bayesian theory and Markov chain Monte Carlo algorithm is also considered as another approach to calculate the short-term extreme response for the two-parameter Weibull distribution and generalized Pareto distribution.

Markov chain Monte Carlo (MCMC): The MCMC is a method to sample from a distribution and to provide a sequence of the sample data in a chain or the so-called parameter space, while, the Bayesian theorem is a theory for interpreting the observed data. The combination of MCMC method and Bayesian theory made a powerful tool that revolutionized data analysis in all scientific domains (Sharma, 2017).

Let $X_{m_1}, X_{m_2}, \ldots, X_{m_n}$ be random variables where the past, and future states are independent, then a Markov chain sequence can be written as (Sharma, 2017):

$$\begin{aligned} p_{\mathrm{MCMC}}(X_{m_{n+1}} = x_m | X_{m_1} = x_{m_1}, X_{m_2} = x_{m_2}, \ldots, X_{m_n} = x_{m_n}) \\ = p_{\mathrm{MCMC}}(X_{m_{n+1}} = x_m | X_{m_n} = x_{m_n}) \end{aligned} \tag{21}$$

where p_{MCMC} refers to the probability density function. Predicting the conditional distribution of $X_{m_{n+1}}$ depends only on the present state, X_{m_n}, rather than on the future or the past. This feature particularly makes the MCMC method a strong tool for predicting the future performances by requiring only a small data set Sharma (2017), and Hobson et al. (2010). This chain is constructed by the transition probabilities of one state to another which can be considered as both discrete and continuous form. The transition probability density which can be defined for a continuous state space is given as (Sharma, 2017):

$$K(x_m, y_m) = p_{\mathrm{MCMC}}(X_{m_{n+1}} = y_m | X_{m_n} = x_m) \tag{22}$$

where K is called the transition kernel.

Ensemble and affine invariant sampling: One way to construct the proposal distribution for the transition kernel is the ensemble and affine invariant sampling (i.e. the generalized case of the Gibbs sampling, cf. Sharma (2017) sections 3.3 and 3.6). In this approach, multiple chains work in parallel while interacting with each other to adapt the proposal density. More importantly, the Markov chain property is not violated by using the information available in the ensemble to adapt the proposal distribution. The highlights of this method can be summarized as:

- It enables a detail balance to be satisfied through conditional sampling i.e. explained in detail in Sharma (2017).
- It results in fast convergence, although it requires the warm up or burn-in, i.e excluding some of the iterations at the beginning of the MCMC run. The computational cost of the warm-up grows linearly with the number of walkers.

Likelihood function: To establish the Bayesian theory and MCMC method, the likelihood function of the distribution of interest should be defined. To apply this methodology, we only focus on the two-parameter Weibull and GPD models. Note that here we consider the two-parameter Weibull and not the Weibull tail-fit model. The likelihood functions for the two-parameter Weibull given the line force peaks (x_{P_i}), and the GPD considering exceedances of the line force peaks (z_{P_i}) are identified as:

$$L_{\mathrm{Weibull}}(\alpha, k) = \prod_{i=1}^{n} \left(\frac{k}{\alpha} \right) \left(\frac{x_{P_i}}{\alpha} \right)^{k-1} \exp\left[-\left(\frac{x_{P_i}}{\alpha} \right)^{k} \right], \tag{23}$$

$$L_{\mathrm{GPD}}(\alpha, k) = \prod_{i=1}^{n} \frac{1}{\alpha} \left(1 + k z_{P_i} \right)^{-(1/k+1)}. \tag{24}$$

Then, the log-likelihood function of the two-parameter Weibull and GPD are defined as:

$$\begin{aligned} \ln(L_{\mathrm{Weibull}}) = n \ln k - nk \ln \alpha + (k-1) \\ \sum_{i=1}^{n} \ln x_{P_i} - \sum_{i=1}^{n} (x_{P_i}/\alpha)^k, \end{aligned} \tag{25}$$

$$\ln(L_{\mathrm{GPD}}) = -n \ln \alpha - (1 + 1/k) \sum_{i=1}^{n} \ln(1 + k z_{P_i}/\alpha). \tag{26}$$

For the case of $k = 0$ in the GPD model, the log-likelihood function is computed as:

$$\ln(L_{\mathrm{GPD}}) = -n \ln \alpha - \alpha^{-1} \sum_{i=1}^{n} z_{P_i}. \tag{27}$$

Prior probability: The present knowledge about the parameters of interest is expressed by the priors. In case the prior knowledge about the parameters of interest is not available or cannot be obtained, a non-informative prior may be used. For the two-parameter Weibull model, the non-informative Jeffreys prior is used for both parameters (i.e. shape and scale) following theorem (Jaynes, 1968; Sun, 1997; Guure et al., 2012; Erto and Giorgio, 2013):

a. Jeffrey's prior is defined as the squared root of the determinant of the Fisher information matrix, $\Pi_R(\alpha, k) \propto \sqrt{Det(\Sigma)}$.
b. The reference prior is the same for α and k parameters, and can be assumed as $\Pi_R(\alpha, k) \propto 1/(\alpha k)$.

For the GPD model, the Jeffreys prior for the scale parameter is considered, while for the shape parameter, a log-normal distribution on $\exp(k)$ is considered as follows:

$$\pi_R(k) = \frac{1}{\exp(k)\sqrt{2\pi}} \exp\left(-\frac{k^2}{2}\right). \tag{28}$$

The parameters of this log-normal distribution are chosen so that the prior becomes almost non-informative for a common range of the shape parameter, i.e. $-0.5 < k < 0.5$.

Note that one might have to check different prior distributions and observe the convergence of the model before finalizing the choice of the prior for the GPD model. For instance, Martín et al. (2022) used the type I Pareto for the shape parameter. Also note that in this study for the GPD model, we do not consider the threshold (u) as a variable to be estimated, and simply we identify the threshold from observing the mean residual life plot as explained in Section 2.5.2, the same as Castellanos and Cabras (2007) who used a fixed threshold.

***Posterior probability*:** The posterior describes the degree of belief in the parameters of interest and is defined as Hobson et al. (2010):

$$p(\theta|x_P) = \frac{p(x_P|\theta)p(\theta)}{p(x_P)} \tag{29}$$

where θ represents the parameters of the distribution. Further, $p(\theta|x_P)$ depicts the posterior probability of θ, and $p(x_P|\theta)$ corresponds to the likelihood function. Moreover, $p(\theta)$ is the prior probability distribution that presents the degree of belief from primary knowledge about the data. Finally, $p(x_P)$ is a normalizing constant, i.e. also named as "marginal likelihood" or "the evidence", that ensures the posterior normalization to unity and can be computed as: $p(x_P) = \int p(x_P|\theta)p(\theta)d\theta$. This equation is usually difficult to be analytically solved, and thereby, numerical methods are applied.

***Bayesian evidence*:** An estimation of the Bayesian evidence based on the Laplace approximation is defined according to Gelman et al. (1995) as:

$$g(\theta) \equiv p(x_P|\theta)p(\theta) \tag{30}$$

$$p(x_P|\mathcal{M}) = (2\pi)^{\frac{N}{2}} \frac{p(x_P|\theta^*,\mathcal{M})p(\theta^*,\mathcal{M})}{|g_{\theta\theta}(\theta^*)|^{\frac{1}{2}}} \tag{31}$$

where θ^* are the parameter values for which $g_{\theta\theta}(\theta)$ is maximum, and N is the number of data points. Also, $g_{\theta\theta}$ is:

$$g_{\theta\theta}(\theta^*) = -\frac{\partial^2 \ln(p(x_P|\theta^*,\mathcal{M})p(\theta^*,\mathcal{M}))}{\partial\theta^2}|_{\theta=\theta^*} \tag{32}$$

which for the two-parameter Weibull and GPD model is a 2×2 matrix. This approximation is especially useful when the posterior can be approximated as a Gaussian distribution around θ^*. Then, the Bayes factor is derived as, Sharma (2017), and Trotta (2017):

$$B_{01} = \frac{p(x_P|\mathcal{M}_0)}{p(x_P|\mathcal{M}_1)} \tag{33}$$

where $p(x_P|\mathcal{M}_0)$ is the marginal likelihood for the initial model, and $p(x_P|\mathcal{M}_1)$ is the marginal likelihood for the secondary one. Here, the Bayesian evidence is computed to investigate the appropriateness of each model.

***Implementation and Python emcee package*:** In this work, Python with emcee package is used to perform this analysis. The implementation is summarized as the following steps:

i. The peaks of line force are considered the same as the first step (i.) of the Weibull tail-fit method.
ii. The log-likelihood function, prior probability, and posterior probability are defined to be used in the affine ensemble sampler for both two-parameter Weibull and GPD models.
iii. The number of walkers is chosen as 100. The sensitivity to the number of walkers in the analysis has been studied and 100 number of walkers is concluded to be sufficient for both models.
iv. Random starting values are generated around the first guess for all parameters for different chains. Note that the initial guesses for the inference on parameters do not require to be accurate, since the model should be able to converge and find the posterior probability regardless of accurate starting positions.
v. Next, the length of the chains is set to be 800. The minimum acceptable number of independent samples is estimated as $N_t/2\tau$ (Sharma, 2017) for each parameter in each model, where N_t is the total number of samples and τ is the auto-correlation time. The stretch move and the differential evolution move within emcee package are defined for the Weibull and GPD model, respectively.
vi. The length of the burn-in for each parameter is chosen through visual inspection of the burn-in plot. In this approach, the MCMC sampler is run following the steps explained above, then each parameter value is plotted for all chains as a function of the position in the chain to find the length of burn-in.
vii. After setting the burn-in length value, the iteration is continued until it reaches the convergence based on the auto-correlation time under the condition that the minimum number of independent samples is reached for each parameter.
viii. In order to compute the parameters mean, median, and credence region of 68% from the quantiles, a flattened chain is constructed by dismissing the burn-in section of the chains.
ix. The corner plots showing the marginalized posterior probability of the parameters are plotted in one and two dimensional parameter space. The GOF plots are also constructed to assess the appropriateness of the fitted model based on the parameters mean value.
x. The Bayesian evidence, i.e. showing which model is preferred by the data and how significant the preference is, is computed as a metric to compare the models. For this purpose, the Laplace approximation is chosen and the posterior is approximated with a second order Taylor expansion around the parameter values with the maximum probability.

2.6. Long-term extreme response analysis

The long-term extreme response analysis gives an understanding of the design response for an offshore system according to the expected loads and response of the system during its deployment life for a particular environmental condition. The long-term analysis may be accomplished by the two well-known methods of full sea state and contour approach to predict the design response.

The long-term full sea state approach provides an accurate and rigorous long-term response at the cost of onerous and extremely expensive computational time. This approach represents the expected long-term response distribution that requires a large number of sea states (H_s and T_p) obtained from both inside and around the environmental contour line, and the long-term response distribution can then be computed as (Muliawan et al., 2013; DNV, 2014; Coe et al., 2016):

$$\bar{P}_{lt}(x) = \int_{h_s}\int_{t_p} \bar{P}_{st|H_s,T_p}(x|h_s,t_p)p_{H_s,Tp}(h_s,t_p)dt_p dh_s \tag{34}$$

where $p_{H_s,Tp}$ expresses the occurrence probability distribution of a specific sea state. Further, $\bar{P}_{st|H_s,T_p}$ is the short-term survival function of the response (X) (e.g. mooring line, or bending moment) or the so-called complimentary cumulative distribution function (CCDF), and it is defined as:

$$\bar{P}_{st}(x) = p(X > x) = 1 - P_{st}(x) \tag{35}$$

in which $P_{st}(x)$ is the short-term cumulative distribution function for 1-hour sea states. This analysis may be carried on considering the sea states with different return periods of 1, 25, 50, or 100 years, depending on the engineering design interest for various environmental load conditions.

On the other hand, the contour approach (DNV, 2014; Coe et al., 2018b,a) seeks along the environmental contour for sea states that contribute to the maximum characteristic responses. The process may be explained as: first to compute the short-term extreme response distribution for sea states along the environmental contour; and then taking the expected value (mean) of the distributions to find the sea state which gives the largest response; and finally considering the distribution with the maximum expected value and using a percentile of this distribution as the long-term response. Taking only a few sea states for this analysis makes this approach significantly faster than the full sea state method. However, this approach is prone to some uncertainties and may underestimate the response level variability owing to neglecting various short-term realizations within the environmental contour (DNV, 2014). To account for this variability, a correction factor may be applied in this method. For instance, Ren et al. (2015), Muliawan et al. (2013) suggested multiplying the expected (mean) value from the short-term extreme distribution by a correction factor of 1.3 that is computed based on comparing the long-term full sea state responses with the corresponding ones from the contour approach. Alternatively, one may only consider a higher percentile of the selected short-term extreme distribution to compensate for this uncertainty (DNV, 2014; Coe et al., 2018b).

The design sea state approach and the design wave approach are two other examples for obtaining the design response of a system. For instance, unlike the contour approach that utilizes the joint probability distribution, the design sea state approach uses a single one-dimensional distribution, i.e. typically the significant wave height distribution. Following that, given the return period of interest (e.g. 50 or 100 years) the expected significant wave height for the desired return period is computed (e.g. $H_{s,50}, H_{s,100}$). Further, the spectral periods (e.g. peak period, T_p, zero-crossing period, T_z, or energy period, T_e) are achieved from the spectral moment equation, $m_n = \int_0^\infty f^n \tilde{S}(f) df$, by knowing the data gathered for the site of interest and the empirical relation for the spectral density function, $\tilde{S}(f)$, (e.g. JONSWAP, Pierson–Moskowitz, or Bretschneider spectrum). Finally, the design response of the system is acquired through a set of simulations for the related sea state realizations (e.g. $H_{s,50}, T_{p_{\min}} < T_p < T_{p_{\max}}$) (DNV, 2014). The design wave approach expands the previous approach by squeezing the wave conditions to either a single regular (monochromatic, harmonic) wave, or a focused wave. The wave height for the regular wave is taken as e.g. $H_{s,100} = 1.9H_s$, knowing the significant wave height of interest for a particular return period. The value 1.9 comes from the assumption that the wave height follows the Rayleigh distribution during storm conditions (Veritas, 2010; Yu et al., 2015). Eventually, the spectral density and consequently the largest response of the device is attained similar to the design sea state approach.

Here, only the full sea state approach and the contour approach have been studied.

2.7. Probabilistic failure

In the deterministic design approach, the load safety factor suggested by the international standards is to be multiplied with the calculated load from the long-term extreme response. Three environmental load factors (γ_f) of 1.35, 1.0, and 1.1 are suggested for the analysis of the ultimate limit states (ULS) by intentional standards corresponding to the extreme, accidental, and abnormal environmental load conditions, respectively, (DNVGL, 2015; Buckland et al., 2021). To acquire the total load safety factor, the environmental load factors should be multiplied with the site factor (γ_s) ranging from 1.0 to 1.25. Safety factor of 1.0 is considered when several years of measurements are available for the deployment site. Whereas, the site factor of 1.05 is for one month of measurement, and safety factor of 1.25 is for an incomplete measurements at the site (DNVGL, 2015). Note that instead of considering the site factor (γ_s), one can directly consider different level of uncertainties for each environmental parameter such as wave, water level, etc. to compensate for the site data inaccuracies (DNVGL, 2015). Here, the 50-year environmental contour is constructed based on 15.4 years of available data. Therefore, the site factor of 1.0 is adopted for this study. Note that for the simplicity of the analysis, the uncertainties within the simulations are neglected.

Nevertheless, the deterministic approach using a safety factor is not adequate to quantify the safety and reliability of a device. With this approach, one cannot simply answer how safe and reliable the design is, or if the device will fail and if so, how often. To be able to answer these questions, a probabilistic analysis is necessary. Here, we describe a simple probabilistic approach considering only the stochastic properties of the yield stress of the material. Note that we do not consider the uncertainties within all design parameters, e.g. material surface quality, geometrical dimension, and so on.

Here, the probability of failure is quantified using the statistical yield stress properties of a shipbuilding high-strength steel. The log-normal distribution is suggested by Veritas (1992) and Hess et al. (2002) as an appropriate distribution for the yield stress of such material. In this study, the mean (μ) and coefficient of variation ($CV = \sigma/\mu$ in which σ is the standard deviation) for the yield stress data of high-strength steel are taken as $\mu = 1.1 s_y$ and $CV = 0.08$, i.e. suggested by VanDerHorn and Wang (2011), where s_y is the nominal (ruled) value of the yield stress. The probability density function of the log-normal distribution is:

$$p_y(x_y) = \frac{1}{x_y \sigma_l \sqrt{2\pi}} \exp\left(-\frac{\left(\ln(x_y) - \mu_l\right)^2}{2\sigma_l^2} \right) \tag{36}$$

for $x_y > 0$, where x_y is the yield stress, and μ_l and σ_l are respectively the mean and standard deviation of logarithmic values and can be expressed in terms of mean (μ) and standard deviation (σ) of the data as:

$$\mu_l = \ln\left(\mu^2/\sqrt{\sigma + \mu^2}\right)$$
$$\sigma_l = \sqrt{\ln(\sigma/\mu^2 + 1)}. \tag{37}$$

We adopt a traditional design approach by finding the minimum cross sectional area required to withstand the design load of interest given the nominal yield stress of the material. More specifically: $A_{cs} = F_{\mathrm{DL}}/s_y$, where F_{DL} is the design load calculated based on the long-term extreme response. Then, the probability density function of the yield force is:

$$p_{F_y}(x_{F_y}) = p_y\left(\frac{x_{F_y}}{A_{cs}}\right)/A_{cs} \tag{38}$$

The geometry can represent the cross sectional area of for instance shackle which is a component that has shown high tendency to failure in the experimental observations as it is illustrated in Weller et al. (2015) and Thies et al. (2013). Further, for the sake of simplicity, we neglect stress concentration factors for the geometry and we consider a uniform stress distribution across the cross section. Fig. 6 shows the probability failure as the gray shadowed area that is a common area under the PDF of the system response and yield force of the material of interest (i.e. a shipbuilding high- strength steel).

2.8. Numerical and analytical implementation

All the numerical and analytical analyses in this paper are conducted in a standard laptop computer except the full sea state approach analysis which was performed using Uppsala Multidisciplinary Center for Advanced Computational Science (UPPMAX). The following software tools are used in this paper: The buoy and PTO are designed and assessed by the computer-added design software (CAD). The mechanical integrity is evaluated using a simple finite element method (FEM) within the CAD software. The WEC-Sim code (Ruehl et al., 2021) in MATLAB is used to simulate the WEC in three degrees of freedom, i.e. surge, heave, and pitch motion. The WAMIT software (Lee and

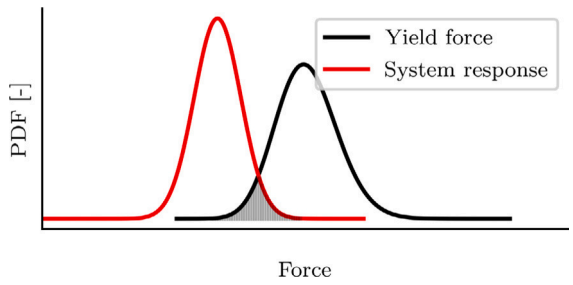

Fig. 6. The red curve represents the long-term extreme PDF of the system response, while the black curve displays the PDF of the yield force for the material of the interest. The shadow gray area demonstrates the probability of failure.

Newman, 2013) is utilized to derive the hydrodynamic coefficients required for WEC-Sim. The outer surface of the buoy is meshed using the Rhino 3D modeller software (Rhinoceros, 2021), to provide the geometry file for the computation of the non-linear buoyancy and Froude–Krylov wave excitation in WEC-Sim. For the contour approach, one week of simulation is performed for the WEC-Sim model to run 120 sea state configurations (i.e. six sea states around the environmental contour × 20 seeds each = 120 configurations). Each configuration has a runtime of about 657 s (i.e. considering 1-hour storm time for a full-scale system × $30^{0.5}$ ≈ 657 s for the 1:30 scaled model using Froude scaling). Whereas, for the full sea state approach, each sea state configuration takes a significantly shorter time of 12 min using 20 cores on UPPMAX cluster. Following this, to study the sensitivity of the full sea state approach to the number of sea states, three different number of configurations, i.e. 180, 360, and 720 sea states, are performed which adds up to 1260 simulations in total. The statistical analysis is carried out by both MATLAB and Python. The short- and long-term analyses are heavily inspired from the WDRT code (Coe et al., 2018a) and adapted for the analysis described in this study. The Bayesian theory and Monte-Carlo algorithm for the short-term extreme response is implemented in Python using the emcee package.

3. Results

3.1. Data realization

The force data is clustered based on the zero up-crossings of the surface elevation. Each cluster contains the time period between two consecutive zero up-crossings of the surface elevation, and then the force peaks are chosen as the maximum of the force data in each cluster. Fig. 7 shows a few seconds of the line force data for sea state 7 which has the highest significant wave height ($H_s = 0.24$ m). When the WEC is operating without the end-stop compression during a calm operation, the line force varies between around 10 N and 30 N with a mean value of around 20 N representing the weight of the PTO, and amplitude of 10 N representing the PTO, pulley, and other internal friction forces. To keep the focus and obtain a better fit for the upper tail of the distribution, only the force peaks above 39 N are considered for the Weibull tail-fit and two-parameter Weibull models in the computation of the long-term extreme response using the contour approach. This value is chosen so to exclude the small force variations in all sea states along the contour. Note that these assumptions are considered for the Weibull models as well as the calibration of the WEC-Sim model, while the Generalized Pareto model used in both contour and full sea state approaches uses the whole force peak data to find the threshold for each sea state. Fig. 8 shows the PDF histogram of the whole force data for the sea state 7. The largest content is associated to the forces below 39 N, with two distinguished peaks indicating the frictional behavior of the PTO during the downward and upward motions of the translator.

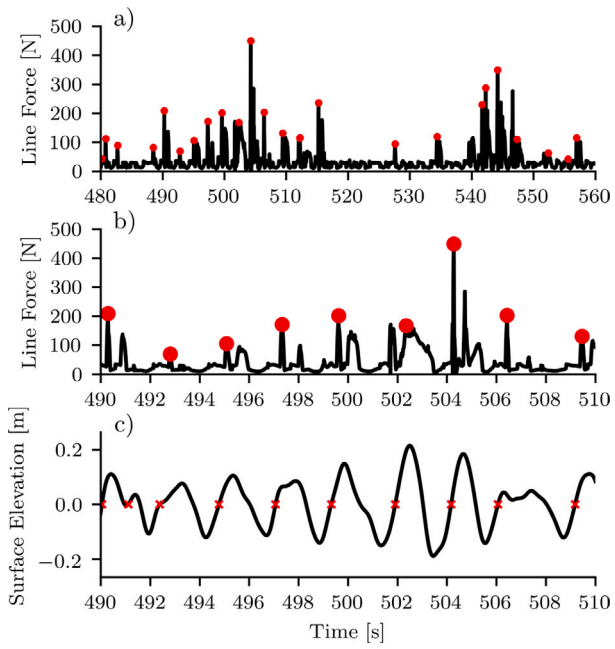

Fig. 7. Force data for sea state 7 from WEC-Sim model for a few seconds is shown in (a). Further, (b) shows the zoomed data between 490 s to 510 s with the selected peaks marked as red circles. The surface elevation with zero up-crossings are shown in (c).

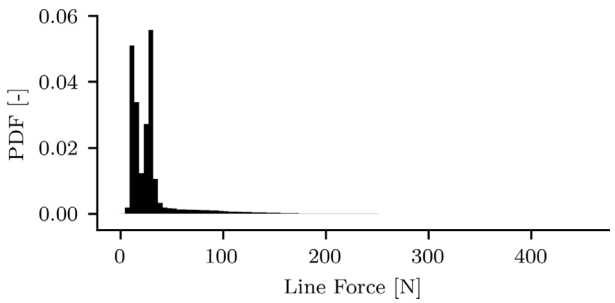

Fig. 8. The PDF histogram of the line force data obtained from the WEC-Sim model for sea state 7.

3.2. WEC-Sim calibration

The wave tank experiments are prone to some uncertainties that are not straightforwardly captured. For instance, although the stroke length has been checked regularly during the experiment, extreme end-stop compression and the existence of a friction PTO can cause gradual deviations in the stroke length during the course of the experiment. In addition, and even though difficult to measure, the energy dissipation during the end-stop impact should be accounted for when modeling the end-stop module. To this end, the WEC-Sim model is further calibrated to achieve a similar response to the experiment by adjusting the end-stop damping parameter which is modeling the dissipative losses during the end-stop impact. A sensitivity study is performed to find the best parameter value for the end-stop damping, see Fig. 9. The optimum damping value is found to be 2500 Ns/m. Although increasing the damping to 4500 Ns/m shows a closer fit to the experimental CDF, observing the force data in the time domain shows that high end-stop damping values produce unrealistic compressive line force after end-stop engagement. By computing the critical damping of the system (i.e. $c_c = 2\sqrt{km}$ where k and m are the spring stiffness and mass, respectively) and damping ratio (i.e. $\zeta = c/c_c$ where c is the viscous damping) (Balachandran and Magrab, 2018), the end-stop viscous

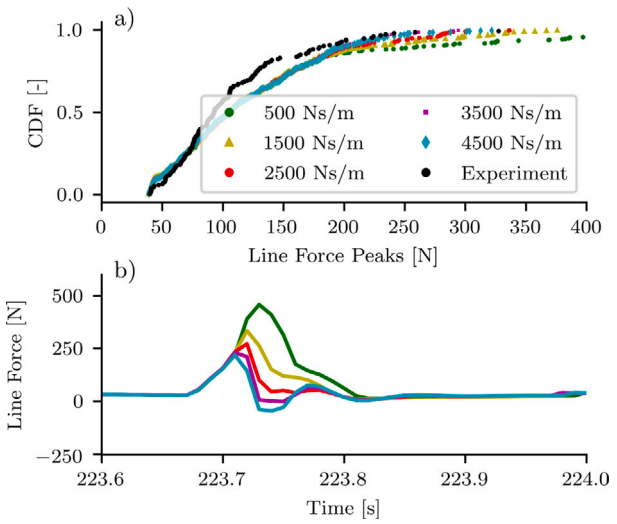

Fig. 9. (a) shows the sensitivity of the peak force CDF to the damping parameter of the PTO end-stop, and (b) shows the line force during a few milliseconds in the event of end-stop compression for different end-stop damping values for the 2-hour simulation of sea state 6. As the damping value increases, the line force becomes unrealistically negative (i.e. the flexible rope (line) cannot physically induce compressive forces).

damping value in the simulation represents an over-damped system. Note that this damping value of 2500 Ns/m for the end-stop is rather a simulation parameter to more accurately replicate the behavior of the real system.

Fig. 10 compares the CDF of the force peaks from the experiment and WEC-Sim model for sea states 5a, 6, and 8. In general, WEC-Sim appears to replicate the experimental distribution fairly well, and since the simulation duration (including all seeds) is longer than the experiment, it is expected to encounter some larger peaks in the numerical results. The exception is sea states 9 and 10 (see Appendix) where larger peak forces are seen for the experimental results compared to the WEC-Sim results. Nevertheless, we will later show that these sea states have no influence in determining the long-term extreme response using the contour approach. The fact that the force peaks CDFs for other sea states are in good agreement with the experiment satisfies our purpose with the numerical WEC-Sim model for this study.

3.3. Diagnostic plots for short-term extreme analysis

To assess the appropriateness of each statistical model and their quality of fits, a set of goodness-of-fit plots (i.e. consisted of probability, quantile, return level, and density plots) are considered. The probability plot compares the CDF of the observations (i.e. the line force peaks) to the CDF of the fitted model, while the quantile plot illustrates how well the model estimates the empirical data. The quantile and probability plots present the same information on a different scale, and the perception of information attained from each scale can be substantial. Hence, if an appropriate fit is seen on one scale, it may appear poor on the other. If the suggested model is reasonable for modeling the extreme forces (i.e. corresponding to the upper tail of the data), the quantile and probability plots should follow the diagonal line. The return level plot here demonstrates the return period of a certain force peak value in terms of number of peaks. For instance, in Fig. 11 for sea state 5a, the force peak around 200 N is expected after 10 number of peaks. This plot is often accompanied by showing the return level confidence interval of 95%. This interval gives the range in which the force peaks lie with 95% confidence. The adequateness of the model is shown if the force peaks are located within this confidence interval. The density plot compares the probability density function of the fitted model with the histogram of the line force peaks. The form of histogram may vary significantly depending on the choice of bins, and this diagnostic plot is considered less informative in comparison with the other ones.

3.3.1. Weibull tail fit distribution GOF

Fig. 11 shows overall a reasonable fit for the upper tail distribution of the force peaks where the quantile and probability plots offer adequately linear trend. However, significant deviation between the diagonal line and low force data points in quantile and probability plots can be seen for almost all sea states. In particular, larger disagreement for lower force data points in sea states 8, 9, and 10 is observed which implicates that a larger fraction of data points for these sea states are situated below the set of limits of Weibull tail-fit CDF, c.f. Section 2.5.1, step (iii.). This indicates the inappropriateness of the Weibull tail-fit method for modeling the lower tail of the force distribution as it should be expected.

The curvature of the return level plot implies the existence of an upper bound for the data. In other words, the return level does not have an ever-increasing trend and will be limited by an upper bound. Further, the narrow banded confidence intervals in the return level plots imply a small error in the estimation of the return level for a certain return period.

Looking at the density plots, one should note that the model is fitted to the upper tail of the peaks distribution, i.e. ranging from 65% to 90% of the CDF, which again aims for a proper fit to the upper tail while being neglectful to the lower tail of the distribution.

The PDF and CDF of the peaks and extreme distributions are shown in Fig. 12. The extreme distribution expresses the distribution of the most extreme peaks in each 0.18-hour simulation (i.e. corresponding to 1 h for the full-scale system) for all 20 seeds. Whereas, the peaks distribution is the distribution of all force peaks in all simulation seeds, see Section 2.5.1, step (v.). As sea states become calmer (e.g. sea states 9 and 10), there would be less number of peaks above 39 N, and thereby, the CDF and PDF of the extreme distribution become more similar and closer to the peaks distribution. This figure implies that the extreme distribution and the peak distribution contain similar information for calm weather conditions.

3.3.2. Generalized pareto distribution GOF

As explained in Section 2.5.2, step (ii.), the choice of the threshold for defining the exceedances is made through assessing the mean residual life, shape stability, and scale stability plots, see Fig. 13. These thresholds are further confirmed by looking at the diagnostic plots for a number of different threshold values. In Fig. 13, the 95% confidence interval (i.e. $\mu_{\text{exc}} \pm 1.96\,\sigma_{\text{exc}}$ in which μ_{exc} and σ_{exc} are the mean and standard deviation of the exceedances, respectively) for mean residual life plot is shown by dashed line, while the standard deviation of the shape and scale parameters are displayed by the error bars. These confidence intervals and standard errors provide us with the necessary information to define a suitable threshold for the POT method. As threshold increases in the mean residual life plots, the confidence interval lines are slowly deviating from the mean residual line (i.e. the solid line). This behavior is due to the increase in the variance of the data owing to decrease in the number of exceedances when the threshold is set at higher values. The same trend is seen for the shape and scale parameters and their standard deviations which are computed from "*the observed information matrix*" using the maximum likelihood estimator (MLE). The detailed information about this computation can be found in Coles et al. (2001), section 2.6.4.

Table 2 summarizes the selected thresholds for each sea state. The generalized Pareto distribution (GPD) with a negative shape parameter is appeared to be the best fit for all the sea states.

Fig. 14 shows the diagnostic plots for the POT method. In general, the POT method shows a fairly good agreement for modeling the high force data points, i.e. the large peaks lying on the diagonal line for the probability and quantile plots. Also, the density plots show the model

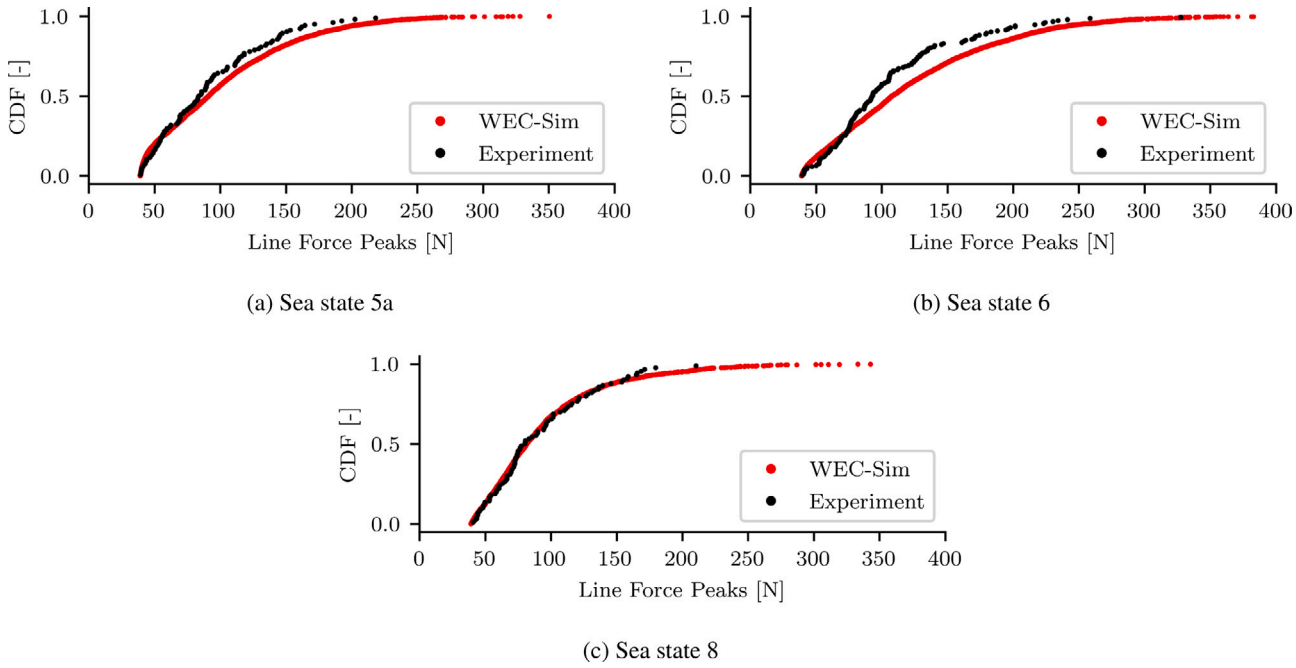

Fig. 10. Comparison of WEC-sim and experimental force peaks CDF.

Table 2
The choice of the threshold for the POT method for each sea state.

Sea state	5a	6	7	8	9	10
Threshold	168	200	234	165	54	48

PDF for each sea state that follows the PDF histogram of the force peaks with great compatibility. Interesting difference between Weibull tail-fit and POT methods is about their upper bound of the return level that is seen to be smaller for the POT method. Note that the probability plots show the CDF of the force peaks above the selected threshold. Thereby, all data points are stacked close to the end of the diagonal line corresponding to high force peaks above the threshold with the CDF values close to one.

As an example, Fig. 15 shows the GPD fit to the upper tail distribution of the force peaks and the extreme distribution for sea state 7 with the significant wave height (H_s = 0.2362 m). Since the GPD is fitted to the exceedances above the threshold, only the very upper tail of distribution of the data (i.e. corresponding to the highest forces peaks) is illustrated which explains the near-zero values for the PDF and the near-one values for the CDF of the GPD model.

3.3.3. GOF of distributions using Bayesian and MCMC

The Bayesian theory and MCMC is applied to mathematically identify the best statistical model that is preferred by the data. Here, we just consider a two-parameter Weibull and a GPD model fitted for sea state 7. The threshold value for the GPD model is taken according to Table 2.

The results of initial burn-in sampling for the two-parameter Weibull and GPD distribution parameters for all chains are presented in Fig. 16. The burn-in length for the GPD model is considered 600 which is larger than the one for the two-parameter Weibull at 150. The convergence of the chains is investigated through auto-correlation analysis (Foreman-Mackey, 2022), where the auto-correlation time is plotted for different number of samples, see Fig. 17. The minimum number of independent samples is estimated as explained in Section 2.5.3, and is chosen where the convergence is approximately achieved, i.e. around 10,000 for the two-parameter Weibull and 1,000,000 for the GPD model indicating a much faster convergence for the two-parameter Weibull model. This relatively slower convergence of the GPD model is mainly due to the large rejection of the steps that do not satisfy $1 + kz/\alpha > 0$ condition in Eq. (16) when $k \neq 0$. The corner plots (see Fig. 18) demonstrate the projection of the posterior probability density functions in one and two dimensional space. This provides useful information regarding the covariance between the parameters, and further shows the marginalized two dimensional distribution of each parameter independently in a histogram form. In the two-parameter Weibull model, the probability distribution of the scale and shape parameter resembles the Gaussian distribution for sea state 7. However, the posterior probability of the shape parameter of the GPD model deviates from the normal distribution which is in contrast to the underlying asymptotic normality assumption in the maximum likelihood estimation approach. The Bayesian approach provides this extra information about the posterior probability of the distribution parameters which could not be extracted otherwise. Nevertheless, this deviation from the normality assumption for the shape parameter here is small and therefore of no concern. Moreover, the more distinguished inclined oval shape in the two dimensional space of the GPD model implies more correlation between the shape and scale parameter compared to the two-parameter Weibull model.

3.3.4. Best method for short-term extreme response

The GPD model using Bayesian theory with MCMC for sea state 7 shows a similar GOF compared to the one obtained in Section 3.3.2. The two-parameter Weibull model using Bayesian theory and MCMC however shows a slightly better fit for the forces above 336 N by looking at the quantile plot in Fig. 19 in comparison to the fit obtained in Section 3.3.1.

The Bayesian evidence provides an excellent and quick way of comparing different statistical models given the same data. This quantifies the appropriateness of each model and minimizes the need for visual investigation of the GOF plots. A number of methods can be considered to perform the Bayesian model inference such as BIC, the Savage–Dickey density ratio, Nested sampling, and Thermodynamic integration, for which the details can be found in Trotta (2017). In this study, the Laplace approximation is chosen for estimating the Bayes evidence to study the model inference. This approach is especially useful when the likelihood function is unimodal and approximately

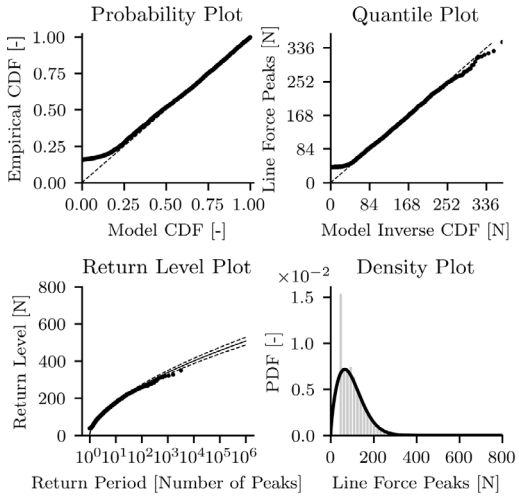

(a) Sea state 5a

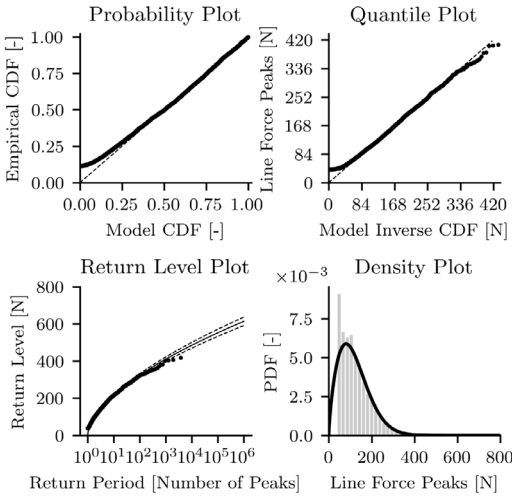

(b) Sea state 6

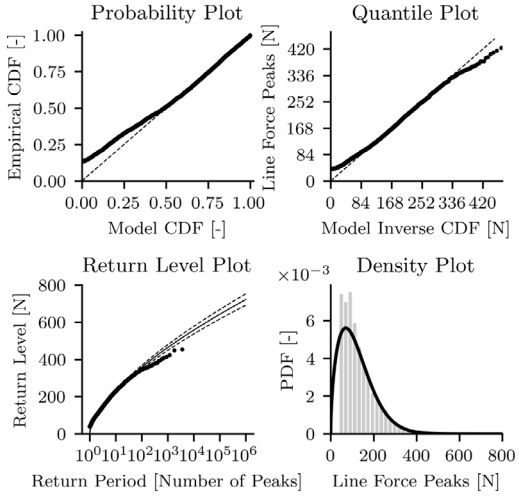

(c) Sea state 7

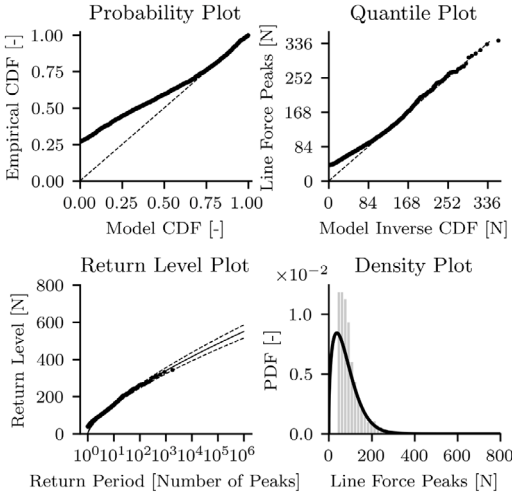

(d) Sea state 8

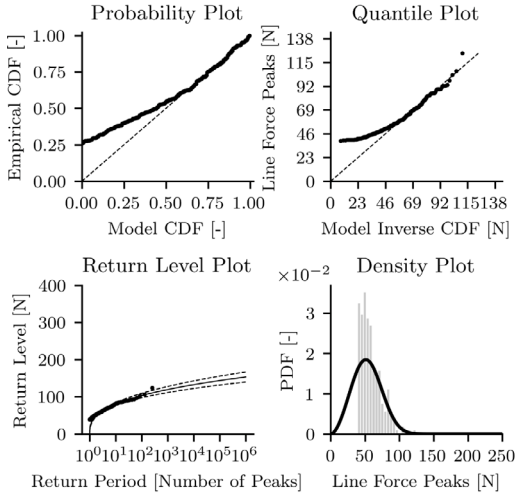

(e) Sea state 9

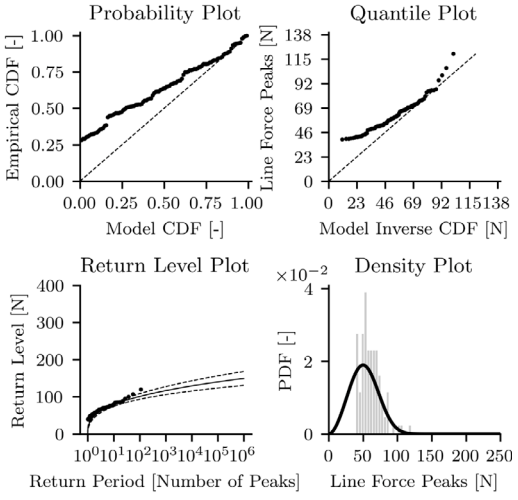

(f) Sea state 10

Fig. 11. Goodness-of-fit plots for the Weibull tail-fit method.

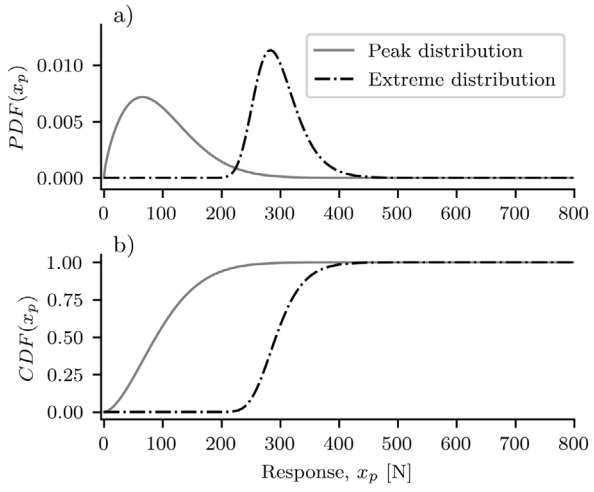

(a) Sea state 5a

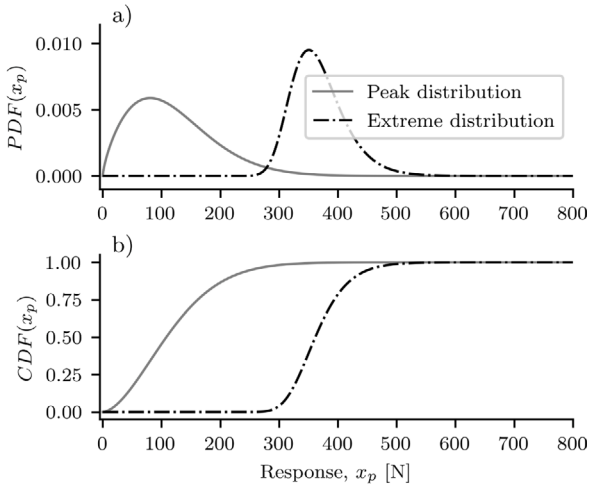

(b) Sea state 6

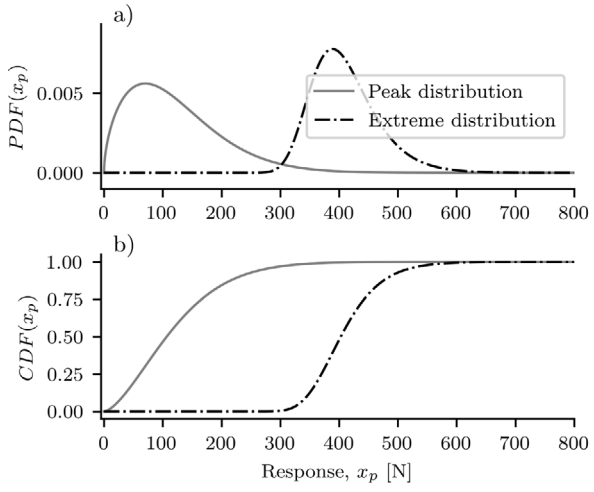

(c) Sea state 7

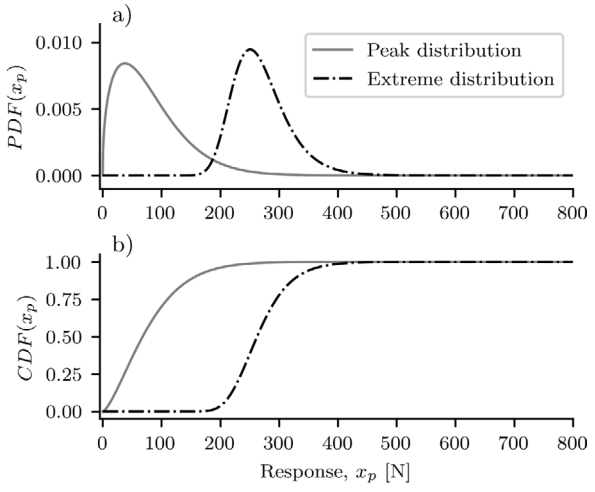

(d) Sea state 8

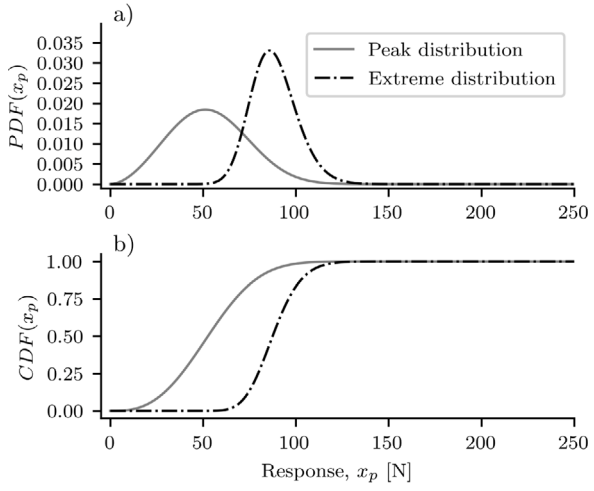

(e) Sea state 9

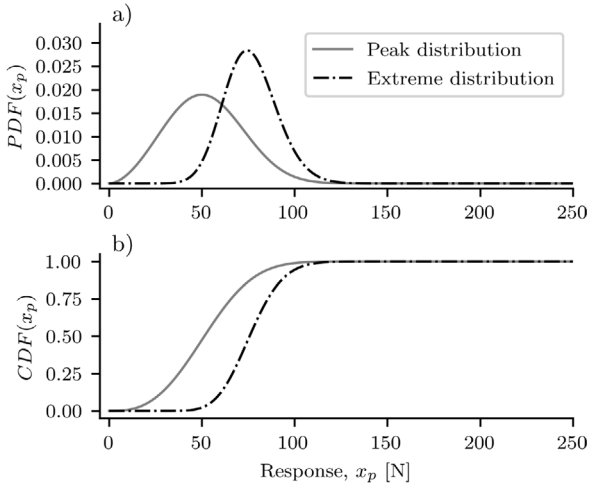

(f) Sea state 10

Fig. 12. Probability density and cumulative distribution functions of peaks and extreme response from Weibull tail-fit method.

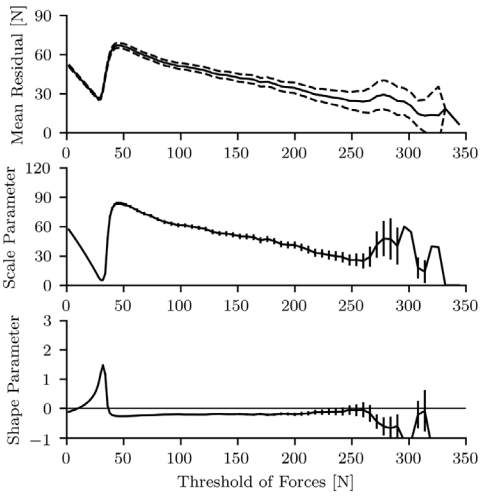

(a) Sea state 5a

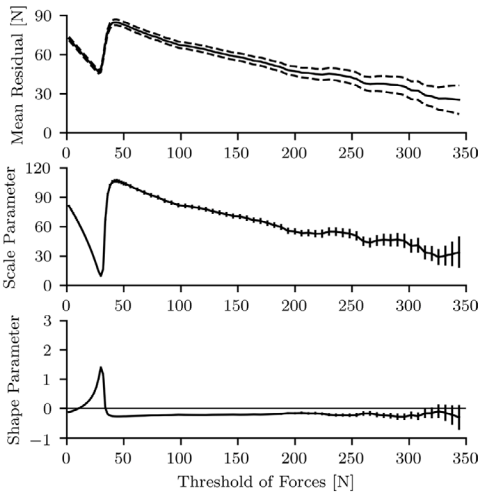

(b) Sea state 6

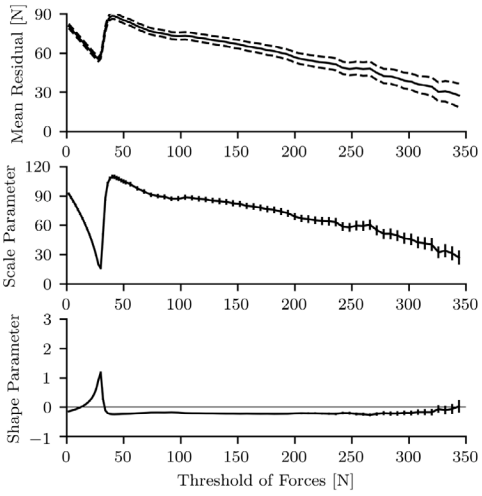

(c) Sea state 7

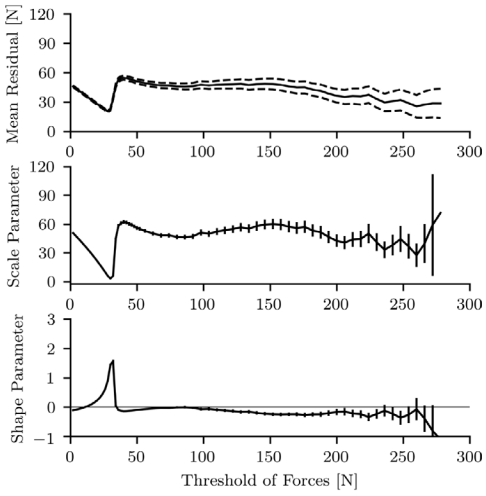

(d) Sea state 8

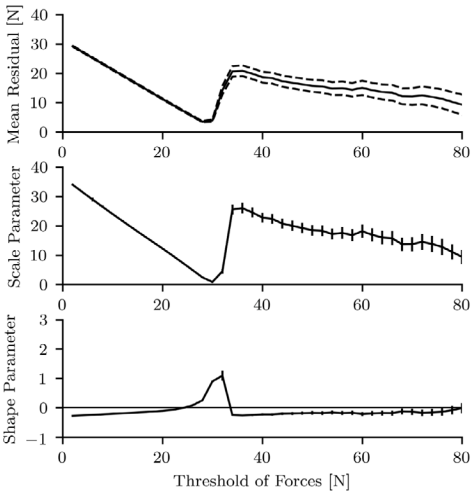

(e) Sea state 9

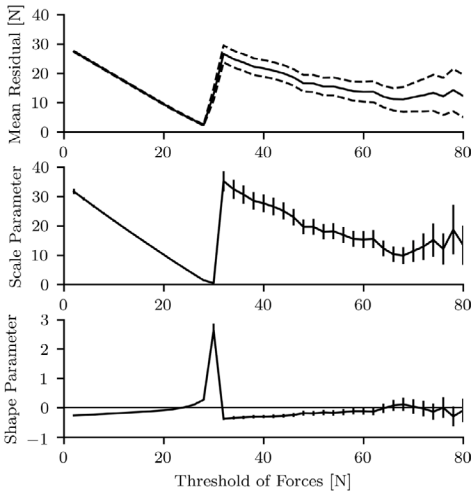

(f) Sea state 10

Fig. 13. Mean residual life as well as scale and shape parameters stability plots for threshold selection in peaks-over-threshold method. The dashed lines in mean residual life plots indicate the confidence interval of the 95%. The error bars in the shape and scale stability plots depict the standard deviation for each parameter.

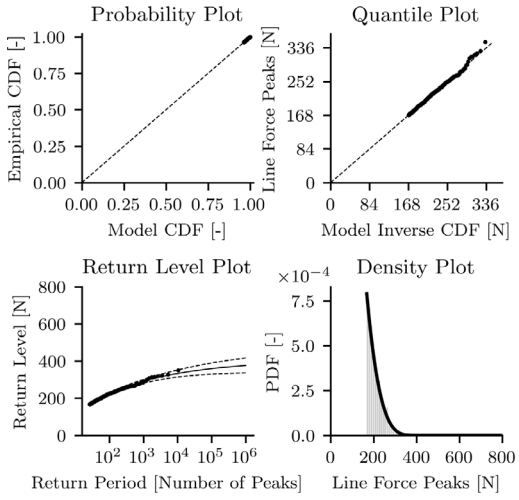

(a) Sea state 5a

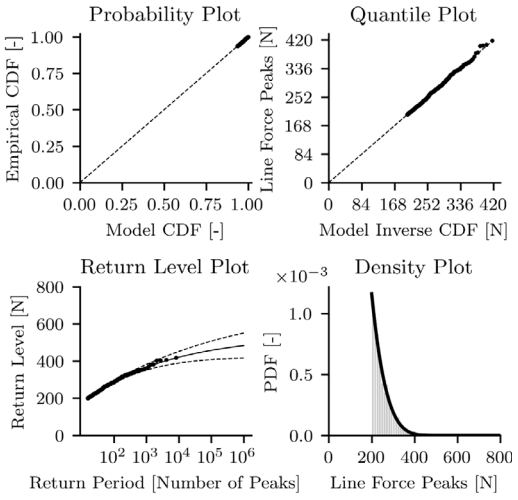

(b) Sea state 6

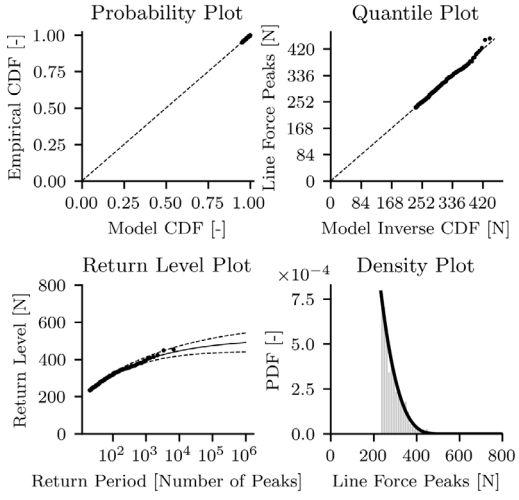

(c) Sea state 7

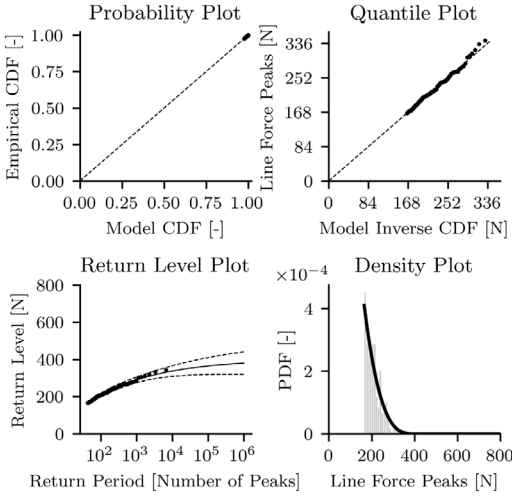

(d) Sea state 8

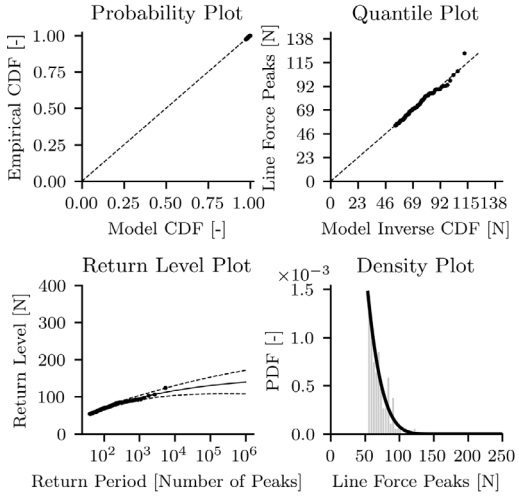

(e) Sea state 9

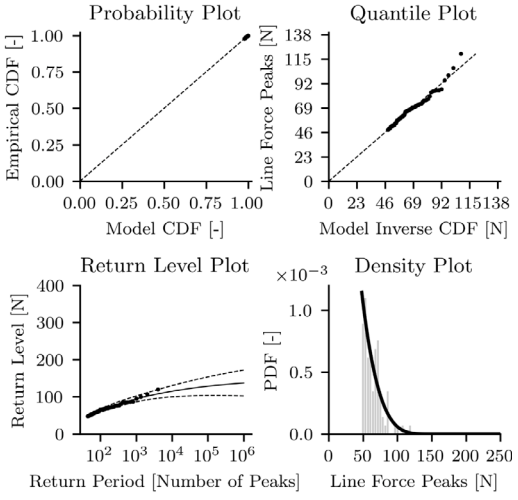

(f) Sea state 10

Fig. 14. Goodness-of-fit plots for peaks-over-threshold method.

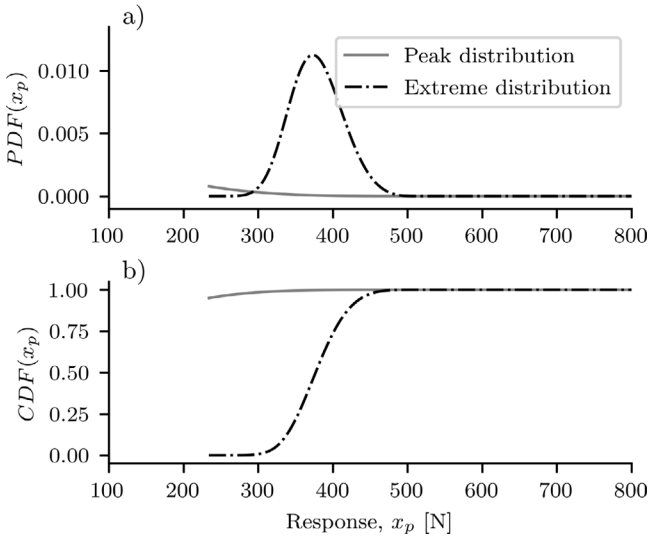

Fig. 15. Probability density and cumulative distribution functions of peaks and extreme response from peaks-over-threshold method for sea state 7.

Table 3
Jeffreys' scale, retrieved from Trotta (2017).

$\lvert \ln B_{01} \rvert$	Odds	Probability	Strength of evidence
<1.0	≲3:1	<0.750	Inconclusive
1.0	~3:1	0.750	Weak evidence
2.5	~12:1	0.923	Moderate evidence
5.0	~150:1	0.993	Strong evidence

Gaussian, Trotta (2017), such as the one studied here. Moreover, this method provides both robust and simple computation compared to e.g. integration in Thermodynamic integration approach or sampling in Nested sampling method which requires a fair number of samples to obtain an accurate solution. Based on Jeffreys' scale, Table 3, the Bayes evidence is evaluated to find the best model.

Table 4 shows the Bayesian evidence in the last column. In order to compare the two-parameter Weibull from Bayesian and tail-fit approaches, the same input data is given corresponding to the upper tail of the data (i.e. above 85% quantile). The negative value of −31.95 for the Bayesian evidence indicates that the second model (i.e. the two-parameter Weibull tail-fit) is strongly preferred by the upper tail of the data based on Jeffreys' scale, Table 3. Note that here we consider the data above 85% quantile to keep the focus on the very tail of the data, however, the Bayesian evidence and hence the preferred model can be affected depending on this limit for the upper tail (i.e. different quantiles). On the other hand, the Bayesian evidence of +0.04, when comparing the GPD model with Bayesian and MCMC ($\mathcal{M}_0$) to the one form MLE ($\mathcal{M}_1$), there is no preference in either of the models. Note that to keep the focus of the paper, we only present the results for sea state 7 in Table 4. Finally, it is not straightforward to compare two different models with two very different input data with the Bayesian evidence metric. For instance, the GPD model that has the exceedances as its input cannot easily be compared with the two-parameter Weibull model which has force peaks as its input. However, comparing the GOF plots for the two-parameter Weibull and GPD models shows an indication for the preference of the GPD model over the others.

3.4. Long-term extreme response and design load

3.4.1. Full sea state approach

Here, the full sea state approach is studied for 180, 360, and 720 sea state samples. The samples are selected from the normal standard space (u-space) between different return periods of 0.001, 0.01, 0.05, 0.1, 0.5, 1, 5, 10, and 50 years. Fig. 20(a) shows the 180 selected sea states in the u-space coordinate system. Between each return period, an equal number of sea states is selected. For instance, when sampling 180 sea states, each ring is radially divided in 20 sections, and one sea state is selected randomly with uniform distribution for each section. Hence, having 9 rings (return periods) in total gives $20 \times 9 = 180$ number of sea states. In the same way 40 and 80 number of sea states samples are selected between each ring when considering 360 and 720 sea state samples, respectively. The sampling strategy adopted here is similar to Coe et al. (2018b). Following that, the sea states are transformed to the T_p and H_s space using the Rosenblatt transformation as shown in Fig. 20(b). Note that the different number of sea state samples are considered to assess the stability of the results in respect to the number of sea states.

Table 4
The estimated parameters for the distributions from different methods for sea state 7. The Bayesian evidence for the two-parameter Weibull models is calculated using the upper tail (i.e. above 85% quantile) of the data for sea state 7.

	Shape	Scale	$\ln(B_{01})$
Two-parameter Weibull from Section 3.3.3 ($\mathcal{M}_0$)	$1.93^{+0.024}_{-0.024}$	$144.26^{+1.34}_{-1.32}$	−31.95
Two-parameter Weibull tail-fit from Section 3.3.1($\mathcal{M}_1$)	$1.56^{+0.021}_{-0.021}$	$134.73^{+1.47}_{-1.47}$	
GPD with Bayesian and MCMC from Section 3.3.3($\mathcal{M}_0$)	$-0.21^{+0.047}_{-0.040}$	$62.29^{+4.38}_{-4.17}$	+0.04
GPD from Section 3.3.2 ($\mathcal{M}_1$)	$-0.22^{+0.043}_{-0.043}$	$62.76^{+4.32}_{-4.32}$	

The joint probability distribution ($p_{H_s,Tp}$ in Eq. (34)) is integrated over each section in each ring in the u-space coordinate system (looking back at Fig. 20(a)) to compute the probability of each corresponding sea state sample. The joint probability density in the T_p and H_s space is shown in Fig. 21.

Then, the full long-term response is computed following Eq. (34) where the short-term survival function or CCDF ($\bar{P}_{st|H_s,T_p}$) is derived based on the GPD model for each short-term extreme distribution. The threshold for all sea states is chosen as: $\mu_{x_p} + 1.4\sigma_{x_p}$, in which μ_{x_p} and σ_{x_p} are the mean and standard deviation of peak forces, with the condition that the number of exceedances is larger than 20 and the shape parameter is negative. If the condition is not fulfilled, the threshold value is incrementally reduced to meet the criteria. Note that although the threshold selection is not as meticulous as it is performed for the contour approach, an extensive study is done to assess the appropriateness of the models and their fits. The diagnostic studies show that good to reasonable fits are achieved for the selected sea states in our model. Note that the Weibull tail-fit model is also investigated, however, the GPD model provides a better fit in comparison. Fig. 22 displays the full sea state survival function where the long-term response of 497 N can be expected after 9.1 years considering the 1:30 scaled system (i.e. corresponding to 50 years in the full-scale system). Since the threshold is different for each sea state, the full sea state survival function can only be defined for the force values above the maximum threshold of all sea states. The comparison of the full sea state survival function for difference number of sea state samples (i.e. 180, 360, and 720) is illustrated in Fig. 23. Coe et al. (2018b) also investigated the full sea state approach and its sensitivity to the number of sea state samples of 50, 100, 200, and 400. They concluded that a higher number of sea state samples leads to a narrower confidence interval, and therefore, the results will be presented more accurately. Here, no significant difference is observed for the number of samples above 180.

3.4.2. Contour approach

The expected (mean) value of each sea state's short-term extreme distribution is illustrated as black circles in Fig. 24. Sea state 7 with the highest significant wave height shows the maximum expected value

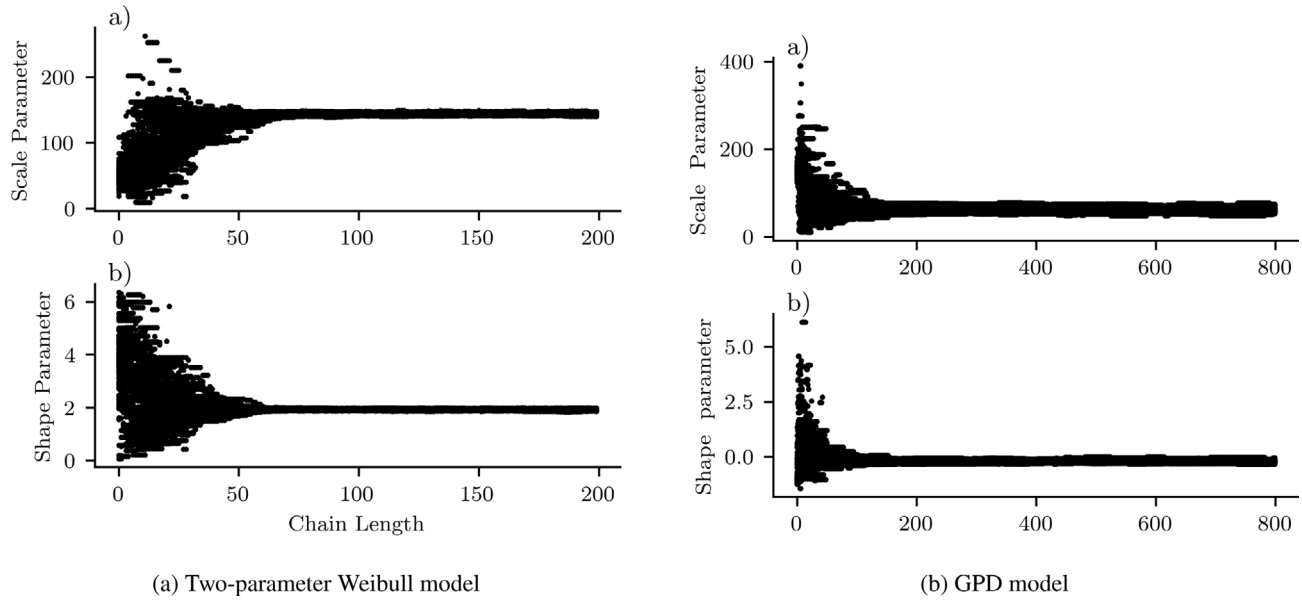

(a) Two-parameter Weibull model (b) GPD model

Fig. 16. Burn-in sampling plots for parameters inference for sea state 7: (a) two-parameter Weibull model, and (b) GPD model.

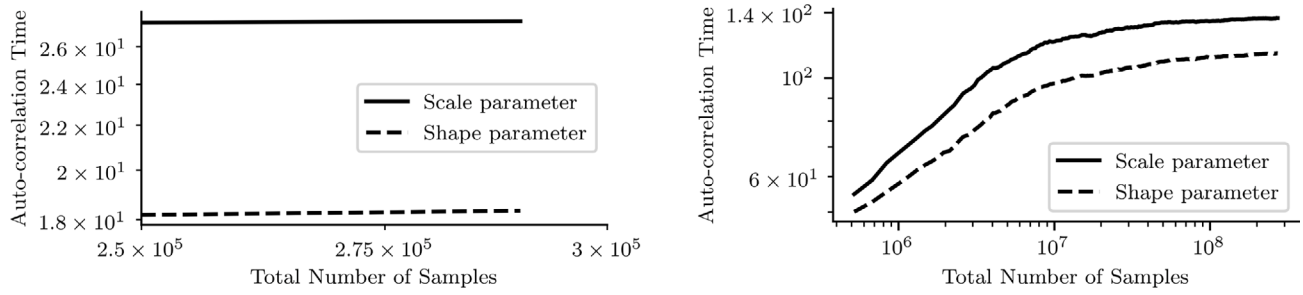

(a) Two-parameter Weibull model (b) GPD model

Fig. 17. Convergence plots for sea state 7: (a) two-parameter Weibull model, and (b) GPD model.

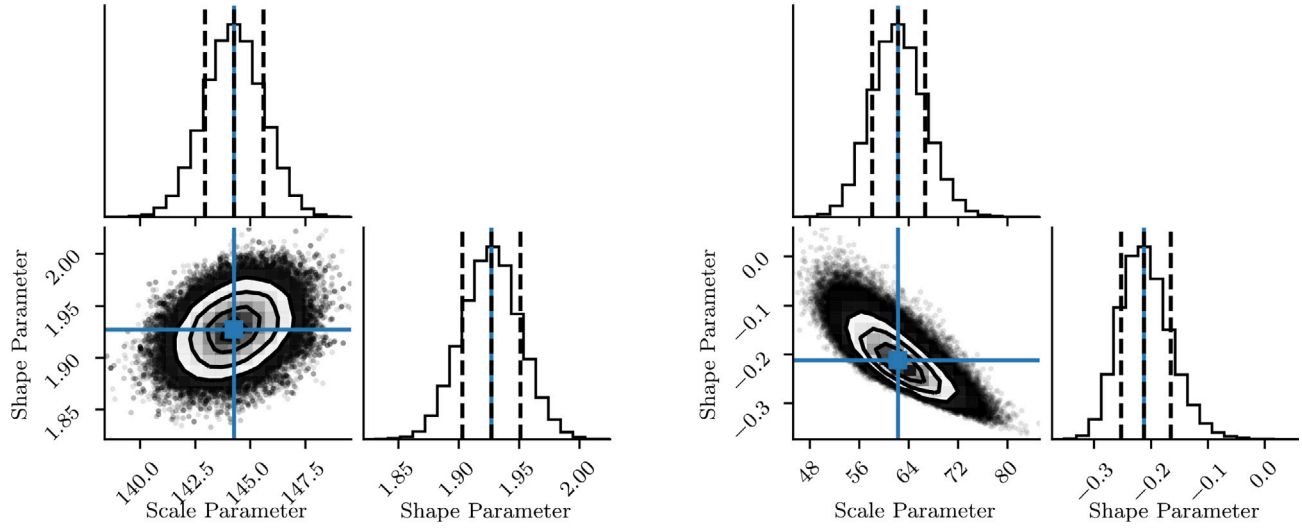

(a) Two-parameter Weibull model (b) GPD model

Fig. 18. Corner plots for the parameters posterior PDF for sea state 7: (a) two-parameter Weibull model, and (b) GPD model.

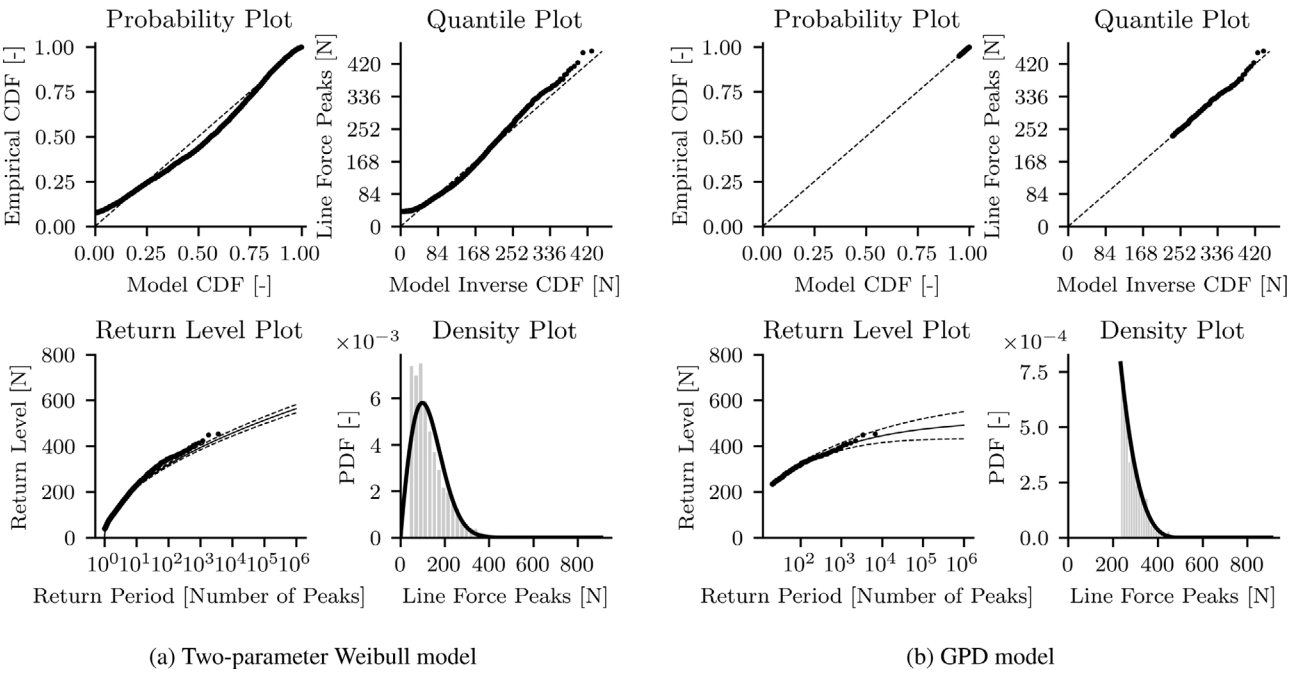

Fig. 19. GOF plots using Bayesian theory and MCMC for sea state 7: (a) two-parameter Weibull model, and (b) GPD model.

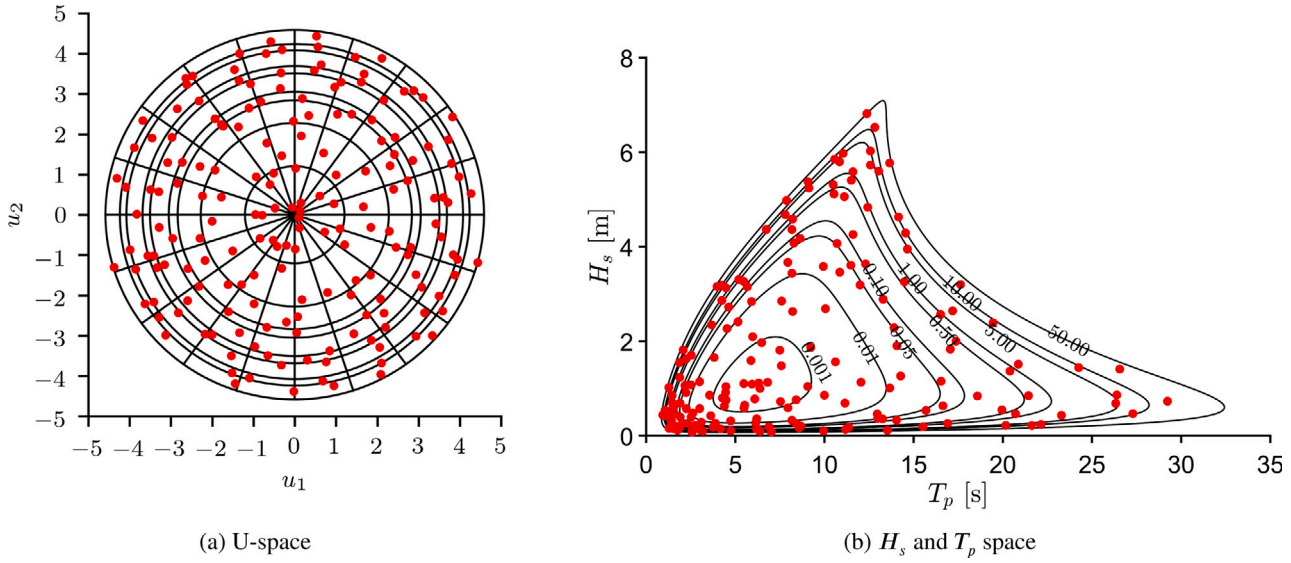

Fig. 20. (a) shows the sampled sea states in the normal standard space. In each ring, 20 sea states are selected which in total adds up to 180 sampled sea states. (b) shows the 180 sampled sea states in the H_s and T_p space. Both (a) and (b) are presented for the full-scale system.

among all sea states. When comparing sea states 5a and 8 with the same significant wave height but different wave period (i.e. $T_p = 1.64$ s for sea state 5a and $T_p = 2.56$ s for sea state 8), a slightly larger peak force (see the last data point in Fig. 10) and expected value of the distribution (see Fig. 24) is seen for sea state 5a compared to sea state 8. Shahroozi et al. (2022) also observed that sea state 8 shows similar and slightly lower maximum line force compared to sea state 5a in the two experimental repetitions, see Fig. 12a therein. A similar trend for the expected values among the sea states can be seen compared to the maximum line force that was achieved during the experiment in Shahroozi et al. (2022), see Fig. 12 therein, where sea states 9 and 10 show the lowest mean values after sea states 5a and 8. Note that the expected values here are computed with a relatively longer simulation time in comparison with the line force obtained during 10-minute experiments.

Following the contour approach explained in Section 2.6, sea state 7 that gives the largest expected value is chosen to find the long-term extreme response. To compensate for the uncertainties for the contour approach, the common practice is to select a higher percentile of short-term distribution.

From the full sea state approach, the full long-term response for the return periods of 1.8, 4.6, and 9.1 years for the 1:30 scaled system (i.e. corresponding to 10, 25, and 50 years in the full-scale system) are considered to compute the corresponding percentiles of each fitted model from the short-term extreme analysis for the most extreme sea state (i.e. sea state 7), see Table 5. Now, by obtaining these percentiles, which are identified in Table 5, one can directly use them to compute the design load only from the contour approach analysis without performing the arduous full sea state analysis. The design load for the return period of 1.8, 4.6 and 9.1 years are also presented in Table 5. For

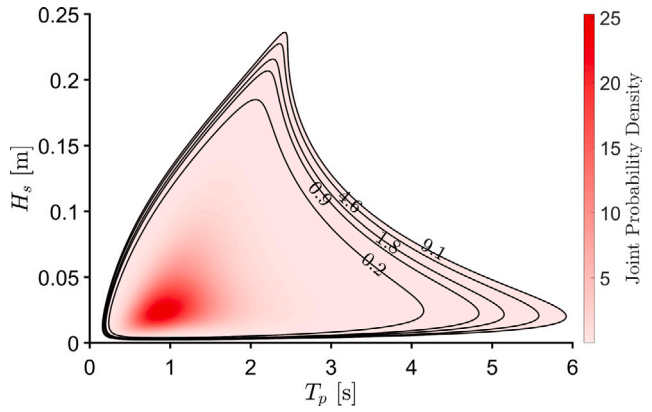

Fig. 21. Join probability density function together with the 0.2, 0.9, 1.8, 4.6, and 9.1 years contour lines in the 1:30 scaled system corresponding to 1, 5, 10, 25, and 50 years contours, respectively, in the full-scale system.

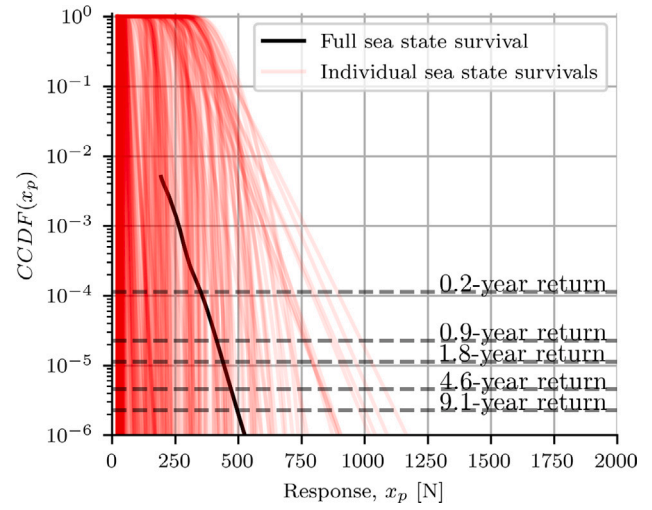

Fig. 22. The survival function for 720 sea states are shown as the solid red lines and the full sea state survival is illustrated as the black line. The dashed red lines represent the survival level for 0.2, 0.9, 1.8, 4.6, and 9.1 years in the 1:30 scaled system corresponding to 1, 5, 10, 25, and 50 years, respectively, in the full-scale system.

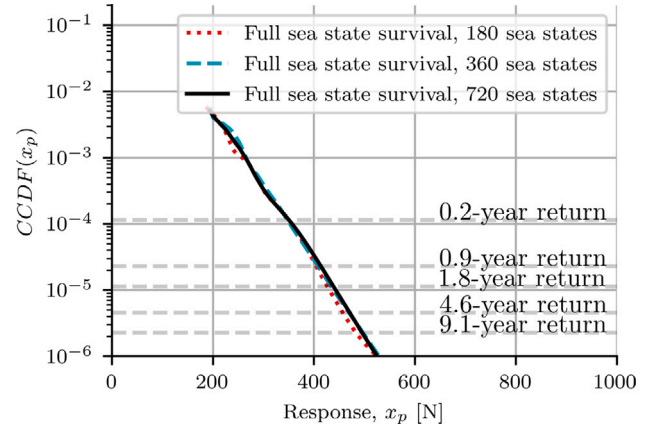

Fig. 23. The full sea state survival function by comparing 180, 360, and 720 sea state samples.

instance, considering the return period of 9.1 years (i.e. corresponding to 50 years return period for the full-scale system), the design load is

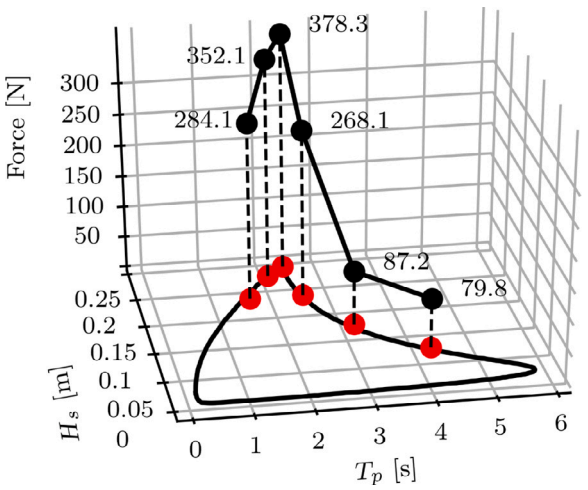

Fig. 24. 3D plot showing the expected value of the extreme distribution for each sea state in black circles from POT method.

670.95 that corresponds to $670.95 \times 30^3 = 18.11$ MN for the full-scale system.

3.5. Probabilistic failure of shackle

The probability of failure is computed for a critical component such as shackle, made of a shipbuilding high-strength steel material. This probability of failure is obtained near zero (0.00012%) considering the long-term extreme response PDF from the full sea state approach together with the yield force PDF (c.f. Eq. (38)). The result represents the probability of the line force exceeding the yield force. Note that the result reported here does not change with the change in the nominal (ruled) yield stress. Further, this result can be interpreted as the probability of failure of a critical component if one considers the design load for 9.1 years (i.e. 497 × 1.35 = 670.95) given a simple design mindset, i.e. the minimum cross sectional area, $A_{cs} = F_{\mathrm{DL}}/s_y$.

4. Discussion and future work

In this study, the WEC-Sim PTO is modeled by a static friction model considering the Stribeck, Coulomb, and viscous components, while the WEC-Sim pulley friction is constructed based on only the Coulomb component. Although the WEC-Sim model provides quite reasonable results for the PTO forces, as aforementioned, it is not always straightforward to model and calibrate a friction-based system accurately. An alternative approach is to utilize the model-free friction compensation schemes using artificial intelligence tools such as neural network, fuzzy logic, and support vector machine (Huang et al., 2019). The main advantages with the model-free friction compensation are estimating the friction more accurately, and relieving the model requirements. Then, the extension of this study would be to develop a model-free friction compensation scheme for the PTO and its implementation in WEC-Sim.

Shahroozi et al. (2022) described different PTO damping cases (i.e. zero to infinite damping) that were considered during the experiment. The authors showed that the zero and infinite damping cases result in the highest peak forces. The analysis performed here is based on one of the damping cases in Shahroozi et al. (2022), i.e. D_1 case therein equivalent to the PTO damping force of 7.4 N. It is of great interest to compute the design load based on other damping cases, however, the zero and infinite damping cases showed strong nonlinearities during experiment due to occurrence of frequent end-stop spring compression (i.e. observed for the zero damping case), overtopping, and wave breaking slamming which are difficult to simulate using

Table 5
Full long-term extreme response (using the full sea state approach) and design load for 1.8, 4.6, and 9.1 years are reported together with the corresponding percentiles from each model for the selected sea states from the contour approach. Note that to compute the design load here, the full long-term extreme response (i.e. 440 N, 471 N and 497 N) should be multiplied with load safety factor of 1.35.

Years return period	1.8 [years]	4.6 [years]	9.1 [years]
Full long-term response	440 [N]	471 [N]	497 [N]
Design load	594 [N]	635.85 [N]	670.95 [N]
Percentile for GPD model from Bayesian and MCMC from Section 3.3.3	95.48	99.55	99.99
Percentile for GPD model from Section 3.3.2	95.49	99.55	99.99
Percentile for two-parameter Weibull model from Section 3.3.3	96.70	98.99	99.65
Percentile for two-parameter Weibull tail-fit model from Section 3.3.1	73.75	86.18	92.32

WEC-Sim. So far, the most accurate modeling technique that can capture most non-linear phenomena is the computational fluid dynamics (CFD) numerical solution method. Despite its accuracy, this numerical method is relatively slow with massive simulation time required for such design load analysis. Other numerical methods are still immature for modeling the non-linearities although they may be computationally less expensive. This indicates a need for alternative methods, e.g. advancements in model-free schemes using artificial intelligence, to be able to accurately model the system response in extreme conditions in a short period of time.

The optimal design of WECs will be achieved when it both satisfies the design requirements considering different limit states, and it is economically viable. Given the fact that the zero and infinite damping cases gave the highest peak line force in Shahroozi et al. (2022), it is expected that a higher design load will be identified for these two damping cases. One way to enhance the survivability and reliability of for example mooring line when looking at line force, without putting a higher demand on the design is to implement a control strategy to adapt the PTO damping depending on the incoming waves to minimize the line force during extreme events. Shahroozi et al. (2022) found that there exists an optimal PTO damping through which the WEC experiences the minimum line force peak. Note that the scaled experiment here is based on the full-scale Uppsala University WEC consisting of a floater connected via rope to a direct-driven linear generator located on the seabed. Hence, the mooring line is one of the critical components in determining the optimal design and therefore this study is dedicated to drive the design load for the line force. For the WEC systems whose mechanical and electrical components are situated in the buoy hull, perhaps even more special attention should be paid for both line forces as well as overtopping forces inserted on the buoy hull when determining the design load. In this case, an optimization scheme may be needed to set a damping value that is neither too high to increase the chance of overtopping phenomenon, nor too low that magnifies other non-linear phenomena such as end-stop spring compression leading to higher line forces.

Previously, first Cruz (2015) and then Neary et al. (2018) suggested a wave energy classification scheme to serve as a tool in designing the WEC considering both extreme load response and design scaling factor. Cruz (2015) classified the site resources through consideration of the significant wave height and energy period. Whereas, Neary et al. (2018) performed the classification considering the annual available energy (AAE) density as:

$$\mathrm{AAE}(T_p) = T_{\mathrm{year}} \Sigma J(T_p) p(J, T_p) \tag{39}$$

where J and $p(J, T_p)$ are the power transport and joint probability of the power transport and wave peak period, respectively, for a distinct partition period band class. Also, T_{year} is the number of hours in a year. Therefore, the total AAE density over all peak periods was given as $\mathrm{AAE} = \Sigma \mathrm{AAE}(T_p)$. Further, the resource classification considered delineation of AAE density by different period bands corresponding to the local sea states to allow designers to specify sites with a high energy concentration. Moreover, different relative risk classes defined by $H_{s_{50}}$ (i.e. the significant wave height with a 50-year return period) and $H_{s_{\mathrm{mean}}}$ (i.e. the mean significant wave height), and the ratio $H_{s_{50}}/H_{s_{\mathrm{mean}}}$ was also distinguished by their resource classification scheme. As a future study of this work, it is of interest to investigate the classification scheme suggested by Neary et al. (2018), and moreover, to consider an adaptive partial safety factor instead of a unify safety factor of 1.35 for all deployment sites, i.e. recommended by the international standards, for each resource class. This is expected to reduce the design and manufacturing costs without jeopardizing the safety of the design.

5. Conclusion

This paper rigorously explores the process of deriving the design load case for the line force of a point-absorber WEC. For this purpose, a numerical 1:30 scaled model (WEC-Sim) is developed and calibrated based on the wave tank experiments for extreme wave conditions derived from the environmental contour with a 50-year return period constructed according to I-FORM hybrid method for the Dowsing site in the North Sea. A simulation time of 1-hour and 20 seeds are considered to generate the response of the system. The short- and long-term extreme responses are obtained based on a set of statistical approaches. The statistical method which provides the best goodness-of-fit in the short-term extreme response analysis is selected for determination of the long-term extreme response and design load case considering ULS and partial load safety factor of 1.35 for extreme environmental conditions. Then, through a probabilistic approach, the probability of failure of a critical component subjected to the line force (such as shackle) for the point-absorber studied here, is described.

The WEC-sim code is found to be a suitable numerical approach to reproduce the system response for irregular waves in the absence of strong non-linearities. It is especially a useful tool when there is a demand for large amount of data augmentation for the analysis such as the one here. However, large deviations between WEC-Sim and the real physical model are expected when non-linearities are high.

The Bayesian theorem and Markov chain Monte-Carlo algorithm is a fairly easy-to-implement approach which provides a mathematical way to quantify the best preferred model by the data. The application of the Bayesian theory and MCMC is particularly beneficial when a small amount of the data is available. Although this aspect is not investigated here, this method is widely used in other disciplines such as astronomy.

Lastly, the environmental design load for the line force considering the partial load safety factor is computed as $497 \times 1.35 = 670.95\ N$ considering full long-term extreme response (i.e. computed from the full sea state approach) for 9.1 years return period for the 1:30 scaled system.

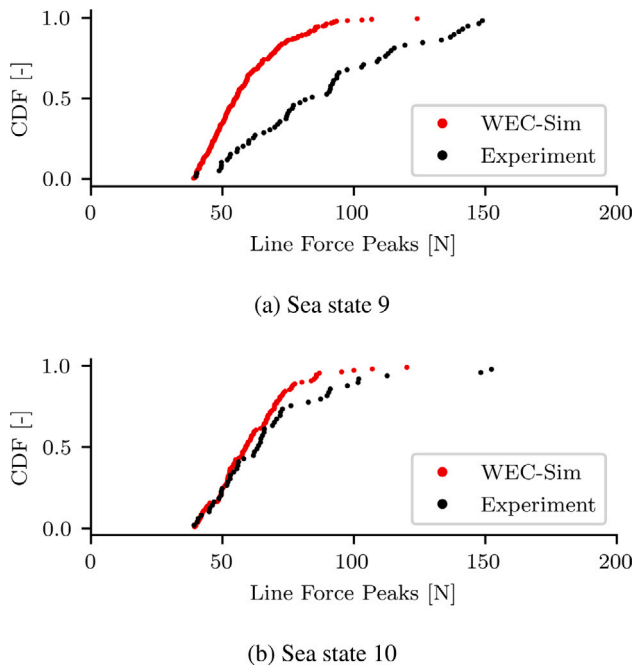

Fig. 25. Comparison of the WEC-sim and experimental force peaks CDF for sea states 9 and 10.

CRediT authorship contribution statement

Zahra Shahroozi: Formal analysis, Writing – original draft. **Malin Göteman:** Formed the initial research questions, supervised the work, reviewed and edited the paper. **Erik Nilsson:** Provided the information about environmental contour and reviewed the paper. **Jens Engström:** Formed the initial research questions, supervised the work, reviewed and edited the paper.

Declaration of competing interest

The authors declare that they have no known competing financial interests or personal relationships that could have appeared to influence the work reported in this paper.

Data availability

At the time of this submission, the data is being used by the group for other publications. In the future, I might be available upon request.

Appendix. Force peaks CDF for sea states 9 and 10

The comparison of the force peaks CDF obtained from the experiment and WEC-Sim is shown in Fig. 25. It is observed that higher surface elevation peaks are obtained in the experiment compared to the simulations which can be a reason for this discrepancy. Another factor that can result in this deviation particularly looking at sea state 9 is the stroke length. If the stroke length is shortened, it leads to excessive end-stop spring compression and therefore high forces. A thorough investigation is made to understand these deviations, however, it is rather difficult to precisely identify and illustrate this discrepancy from the experimental data. Nonetheless, as it is mentioned before, these two sea states do not influence the long-term extreme response from the contour approach in determining the design load.

References

Ang, A.H., Tang, W.H., 1984. Probability Concepts in Engineering, Planning and Desing. Vol. 2.. John Wiley&Sons, New York, USA.

Armstrong, B., de Wit, C., 1995. Canudas," Friction Modeling and Compensation", the Control Handbook. CRC Press.

Armstrong-Helouvry, B., 2012. Control of Machines with Friction, Vol. 128. Springer Science & Business Media.

Armstrong-Helouvry, B., Soom, A., 1992. Control of machines with friction.

Balachandran, B., Magrab, E.B., 2018. Vibrations. Cambridge University Press.

Berg, J.C., 2011. Extreme ocean wave conditions for northern california wave energy conversion device. Sandia Natl. Lab. Doc. SAND 9304, 2011.

Bosma, B., Simmons, A., Lomonaco, P., Ruehl, K., Gunawan, B., 2016. Wec-sim phase 1 validation testing: experimental setup and initial results. In: International Conference on Offshore Mechanics and Arctic Engineering, Vol. 49972. American Society of Mechanical Engineers, V006T09A025.

Buckland, H., Hemmant, J., Meason, J., Gaviglio, H., 2021. An adaptation of design load cases for a wave energy converter. In: Greaves, D. (Ed.), Proceedings of the Fourteenth European Wave and Tidal Energy Conference. EWTEC, University of Plymouth, UK, (ISSN: 2309-1983) pp. 1941–1–1941–5.

Castellanos, M.E., Cabras, S., 2007. A default Bayesian procedure for the generalized Pareto distribution. J. Statist. Plann. Inference 137 (2), 473–483.

Chang, K., 2015. In: Chang, K. (Ed.), Reliability Analysis, in E-Design Computer-Aided Engineering Design. Academic Press.

Chen, M., Xiao, P., Zhang, Z., Sun, L., Li, F., 2021. Effects of the end-stop mechanism on the nonlinear dynamics and power generation of a point absorber in regular waves. Ocean Eng. 242, 110123.

Coe, R.G., Michelen, C., Eckert-Gallup, A., Martin, N., Yu, Y.-H., van Rij, J., Quon, E.W., Manuel, L., Nguyen, P., Esterly, T., Seng, B., Stuart, Z., Canning, J., 2018a. WEC design response toolbox (WDRT). URL: http://wec-sim.github.io/WDRT.

Coe, R.G., Michelen, C., Eckert-Gallup, A., Sallaberry, C., 2018b. Full long-term design response analysis of a wave energy converter. Renew. Energy 116, 356–366.

Coe, R.G., Michelen, C., Yu, Y.-H., Rij, J.V., Eckert-Gallup, A.C., 2016. WDRT: A Toolbox for Design-Response Analysis of Wave Energy Converters. Technical Report, Sandia National Lab.(SNL-NM), Albuquerque, NM (United States).

Coles, S., Bawa, J., Trenner, L., Dorazio, P., 2001. An Introduction to Statistical Modeling of Extreme Values, Vol. 208. Springer.

Commission, I.E., et al., 2019. Wind energy generation systems-Part 3-1: Design requirements for fixed offshore wind turbines. International Standard IEC 61400-3-1, IEC Geneva.

Cruz, J., 2015. WEC classes: Preliminary studies. In: European Wave and Tidal Energy Conference. Nantes, France.

De Wit, C.C., Olsson, H., Astrom, K.J., Lischinsky, P., 1995. A new model for control of systems with friction. IEEE Trans. Automat. Control 40 (3), 419–425.

DNV, G., 2014. Environmental conditions and environmental loads (DNV-RP-C205). Det Norske Veritas AS, Oslo.

DNVGL, 2015. DNVGL-ST-0164: Tidal turbines. DNV GL Bærum, Norway.

Eckert-Gallup, A.C., Sallaberry, C.J., Dallman, A.R., Neary, V.S., 2016. Application of principal component analysis (PCA) and improved joint probability distributions to the inverse first-order reliability method (i-FORM) for predicting extreme sea states. Ocean Eng. 112, 307–319.

Edwards, S.J., Coe, R.G., 2019. The effect of environmental contour selection on expected wave energy converter response. J. Offshore Mech. Arct. Eng. 141 (1).

Erto, P., Giorgio, M., 2013. A note on using Bayes priors for Weibull distribution. arXiv preprint arXiv:1310.7056.

Eskilsson, C., Palm, J., Johannesson, P., Paredes, G.M., 2021. Sensitivity analysis of extreme loads acting on a point-absorbing wave energy converter. In: 14th European Wave and Tidal Energy Conference 5-9th Sept 2021. Plymouth, UK, pp. 1992–1.

Foreman-Mackey, D., 2022. Emcee package. https://emcee.readthedocs.io/en/stable/tutorials/.

Fu, J., Maré, J.-C., Fu, Y., 2017. Modelling and simulation of flight control electromechanical actuators with special focus on model architecting, multidisciplinary effects and power flows. Chin. J. Aeronaut. 30 (1), 47–65.

Gelman, A., Carlin, J.B., Stern, H.S., Rubin, D.B., 1995. Bayesian Data Analysis. Chapman and Hall/CRC.

Guure, C.B., Ibrahim, N.A., Ahmed, A.O.M., 2012. Bayesian estimation of two-parameter weibull distribution using extension of jeffreys' prior information with three loss functions. Math. Probl. Eng. 2012.

Haver, S., 1986. A wave climate description for long-term response calculations. In: Proceedings of OMAE'86. pp. 27–34.

Haver, S., 2002. On the prediction of extreme wave crest heights. In: 7th Int. Workshop on Wave Hindcasting and Forecasting, Banff, Canada. Citeseer.

Haver, S., Winterstein, S.R., 2008. Environmental contour lines: A method for estimating long term extremes by a short term analysis. In: SNAME Maritime Convention. OnePetro.

Hess, P.E., Bruchman, D., Assakkaf, I.A., Ayyub, B.M., 2002. Uncertainties in material and geometric strength and load variables. Nav. Eng. J. 114 (2), 139–166.

Hess, D., Soom, A., 1990. Friction at a lubricated line contact operating at oscillating sliding velocities.

Hobson, M.P., Jaffe, A.H., Liddle, A.R., Mukherjee, P., Parkinson, D., 2010. Bayesian Methods in Cosmology. Cambridge University Press.
Huang, S., Liang, W., Tan, K.K., 2019. Intelligent friction compensation: A review. IEEE/ASME Trans. Mechatronics 24 (4), 1763–1774.
IEC, 2016. Marine energy-wave, tidal and other water current converters - Part 2: Design requirements for marine energy systems. IEC TS 62600-2:2016-08.
Jaynes, E.T., 1968. Prior probabilities. IEEE Trans. Syst. Sci. Cybern. 4 (3), 227–241.
Katsidoniotaki, E., Nilsson, E., Rutgersson, A., Engström, J., Göteman, M., 2021. Response of point-absorbing wave energy conversion system in 50-years return period extreme focused waves. J. Mar. Sci. Eng. 9 (3), 345.
Lampaert, V., Swevers, J., Al-Bender, F., 2002. Modification of the leuven integrated friction model structure. IEEE Trans. Automat. Control 47 (4), 683–687.
Lawson, M., Yu, Y.-H., Nelessen, A., Ruehl, K., Michelen, C., 2014. Implementing nonlinear buoyancy and excitation forces in the wec-sim wave energy converter modeling tool. In: International Conference on Offshore Mechanics and Arctic Engineering. 45547, American Society of Mechanical Engineers, V09BT09A043.
Lee, C., Newman, J., 2013. Wamit–User Manual Version 7.0. WAMIT Inc, Chestnut Hill, Massachusetts.
Martín, J., Parra, M.I., Pizarro, M.M., Sanjuán, E.L., 2022. Baseline methods for the parameter estimation of the generalized Pareto distribution. Entropy 24 (2), 178.
Michelen, C., Coe, R., 2015. Comparison of methods for estimating short-term extreme response of wave energy converters. In: OCEANS 2015 - MTS/IEEE Washington. pp. 1–6. http://dx.doi.org/10.23919/OCEANS.2015.7401878.
Muliawan, M.J., Gao, Z., Moan, T., 2013. Application of the contour line method for estimating extreme responses in the mooring lines of a two-body floating wave energy converter. J. Offshore Mech. Arct. Eng. 135 (3).
Næss, A., Gaidai, O., 2009. Estimation of extreme values from sampled time series. Struct. Saf. 31 (4), 325–334.
Neary, V.S., Ahn, S., Seng, B.E., Allahdadi, M.N., Wang, T., Yang, Z., He, R., 2020. Characterization of extreme wave conditions for wave energy converter design and project risk assessment. J. Mar. Sci. Eng. 8 (4), 289.
Neary, V.S., Coe, R.G., Cruz, J.a., Haas, K., Bacelli, G., Debruyne, Y., Ahn, S., Nevarez, V., 2018. Classification systems for wave energy resources and WEC technologies. Int. Mar. Energy J. 1 (2 (Nov)), 71–79.
Neary, V., Haselsteiner, A., An, R., Ströer, L., Coe, R., Windmeier, K., Ahn, S., 2021. Design load case generator: Web-based tool to determine IEC 62600-2 standard design load requirements. In: Greaves, D. (Ed.), Proceedings of the Fourteenth European Wave and Tidal Energy Conference. EWTEC, University of Plymouth, UK, (ISSN: 2309-1983) pp. 2095–1–2095–10.
Ren, N., Gao, Z., Moan, T., Wan, L., 2015. Long-term performance estimation of the Spar–Torus-combination (STC) system with different survival modes. Ocean Eng. 108, 716–728.
Rhinoceros, 2021. Rhino 7. https://www.rhino3d.com/7/new/.
Ronold, K.O., Hansen, V.L., Godvik, M., Landet, E., Jorgensen, E.R., Hopstad, A.L.H., 2010. Guideline for offshore floating wind turbine structures. In: International Conference on Offshore Mechanics and Arctic Engineering, Vol. 49118. pp. 381–388.
Rosenblatt, M., 1952. Remarks on a multivariate transformation. Ann. Math. Stat. 23 (3), 470–472.
Ruehl, K., Ogden, D., Yu, Y.-H., Keester, A., Tom, N., Forbush, D., Leon, J., 2021. WEC-sim v4.4. http://dx.doi.org/10.5281/zenodo.5608563, Zenodo, URL: https://zenodo.org/badge/latestdoi/20451353.
Sagrilo, L.V., Gao, Z., Naess, A., Lima, E.C., 2011. A straightforward approach for using single time domain simulations to assess characteristic extreme responses. Ocean Eng. 38 (13), 1464–1471.
Sagrilo, L.s.V.S., Naess, A., Gao, Z., 2012. On the extreme value analysis of the response of a turret moored FPSO. J. Offshore Mech. Arct. Eng. 134 (4).
Sagrilo, L.V., Siqueira, M.Q., Ellwanger, G.B., Lima, E.C., Ferreira, M.D., Mourelle, M.M., 2002. A coupled approach for dynamic analysis of CALM systems. Appl. Ocean Res. 24 (1), 47–58.
Shahroozi, Z., 2021. Prediction Horizon Requirement in Control and Extreme Load Analyses for Survivability: advancements to Improve the Performance of Wave Energy Technologies. (Ph.D. thesis). Uppsala University.
Shahroozi, Z., Göteman, M., Engström, J., 2021. Experimental results of force measurements from a scaled point absorbing wave energy converter subjected to extreme waves. In: Greaves, D. (Ed.), Proceedings of the Fourteenth European Wave and Tidal Energy Conference. EWTEC, University of Plymouth, UK, (ISSN: 2309-1983) pp. 1881–1–1881–10.
Shahroozi, Z., Göteman, M., Engström, J., 2022. Experimental investigation of a point-absorber wave energy converter response in different wave-type representations of extreme sea states. Ocean Eng. 248, 110693.
Sharma, S., 2017. Markov chain Monte Carlo methods for Bayesian data analysis in astronomy. Annu. Rev. Astron. Astrophys. 55, 213–259.
Sun, D., 1997. A note on noninformative priors for Weibull distributions. J. Statist. Plann. Inference 61 (2), 319–338.
Swevers, J., Al-Bender, F., Ganseman, C.G., Projogo, T., 2000. An integrated friction model structure with improved presliding behavior for accurate friction compensation. IEEE Trans. Automat. Control 45 (4), 675–686.
Thies, P.R., Johanning, L., Gordelier, T., Vickers, A., Weller, S., 2013. Physical component testing to simulate dynamic marine load conditions. In: International Conference on Offshore Mechanics and Arctic Engineering, Vol. 55331. American Society of Mechanical Engineers, V02BT02A002.
Tjahjowidodo, T., Al-Bender, F., Van Brussel, H., Symens, W., 2007. Friction characterization and compensation in electro-mechanical systems. J. Sound Vib. 308 (3–5), 632–646.
Todalshaug, J.H., Babarit, A., Kurniawan, A., Moan, T., 2011. The numwec project. Numerical estimation of energy delivery from a selection of wave energy converters–final report. Report for the NumWEC Project, Nantes, France.
Tosdevin, T., Giassi, M., Thomas, S., Engstrom, J., Hann, M., Isberg, J., Goteman, M., Ransley, E., Musliedlak, P., Simmonds, D., et al., 2020. On the calibration of a WEC-sim model for heaving point absorbers.
Trotta, R., 2017. Bayesian methods in cosmology. arXiv preprint arXiv:1701.01467.
van Rij, J., Yu, Y.-H., Edwards, K., Mekhiche, M., 2017. Ocean power technology design optimization. Int. J. Mar. Energy 20, 97–108.
van Rij, J., Yu, Y.-H., Guo, Y., Coe, R.G., 2019a. A wave energy converter design load case study. J. Mar. Sci. Eng. 7 (8), 250.
van Rij, J.A., Yu, Y.-H., Tom, N.M., 2019b. Validation of Simulated Wave Energy Converter Responses to Focused Waves for CCP-WSI Blind Test Series 2. Technical Report, National Renewable Energy Lab.(NREL), Golden, CO (United States).
VanDerHorn, E., Wang, G., 2011. A statistical study on the material properties of shipbuilding steels. Sustain. Marit. Transp. Exploit. Sea Resourc. 371–378.
Vanem, E., 2015. Uncertainties in extreme value modelling of wave data in a climate change perspective. J. Ocean Eng. Mar. Energy 1 (4), 339–359.
Veritas, N., 1992. Structural Reliability Analysis of Marine Structures. Det Norske Veritas.
Veritas, D.N., 2010. Recommended practice DNV-RP-C205: environmental conditions and environmental loads. DNV, Norway.
WaveNet, 2022. Wave monitoring network for the United Kingdom. https://www.cefas.co.uk/data-and-publications/wavenet/.
Weller, S.D., Thies, P.R., Gordelier, T., Johanning, L., 2015. Reducing reliability uncertainties for marine renewable energy. J. Mar. Sci. Eng. 3 (4), 1349–1361.
Winterstein, S.R., 1988. Nonlinear vibration models for extremes and fatigue. J. Eng. Mech. 114 (10), 1772–1790.
Wrang, L., Katsidoniotaki, E., Nilsson, E., Rutgersson, A., Rydén, J., Göteman, M., 2021. Comparative analysis of environmental contour approaches to estimating extreme waves for offshore installations for the baltic sea and the north sea. J. Mar. Sci. Eng. 9 (1), 96.
Yu, Y.-H., Van Rij, J., Coe, R., Lawson, M., 2015. Preliminary wave energy converters extreme load analysis. In: International Conference on Offshore Mechanics and Arctic Engineering. 56574, American Society of Mechanical Engineers, V009T09A026.